INTERNATIONAL ATOMIC ENERGY AGENCY
UNITED NATIONS EDUCATIONAL, SCIENTIFIC AND CULTURAL ORGANIZATION
INTERNATIONAL CENTRE FOR THEORETICAL PHYSICS
I.C.T.P., P.O. BOX 586, 34100 TRIESTE, ITALY, CABLE CENTRATOM TRIESTE

SMR.550 - 29

SPRING COLLEGE IN MATERIALS SCIENCE ON
"NUCLEATION, GROWTH AND SEGREGATION IN MATERIALS
SCIENCE AND ENGINEERING"
(6 May - 7 June 1991)

POLYGONISATION AND RECRYSTALLISATION PHENOMENA

J.R. MATTHEWS
Materials and Chemistry Division
Building 10.5
AEA Reactor Services
Harwell Laboratory
11 Charles II Street
London SW1Y 4QP
United Kingdom

POLYGONISATION AND RECRYSTALLISATION PHENOMENA

A Series of 5 Lectures which form part of the Spring College in Materials Science on 'Nucleation, Growth and Segregation in Materials Science and Engineering'

International Centre for Theoretical Physics
Trieste
May 1991

J R Matthews
Divisional Manager, Materials & Chemistry
AEA Reactor Services
HARWELL LABORATORY

CONTENTS

BIBLIOGRAPHY

Individual references are not given in the text but the following sources will provide further reading.

DISLOCATION PATTERNING - EXPERIMENTAL OBSERVATIONS

1. Proceedings of the International Conference on Low Energy Dislocation Structures, Charlottsville, VA, USA, August 1986. Ed D Kuhlmann-Wilsdorf & E A Starke Jr, published in Materials Science & Engineering, 81 (1986), 1-575.

DISLOCATION PATTERNING - MODELLING

2. R J Amodeo. Dynamic Simulation of Dislocation Pattern Formation in Metals during High Temperature Deformation. Res Mechanica, 30 (1990) 1-142.

DISLOCATION PATTERNING - MATERIAL INSTABILITIES

3. Special Issue - Material Instabilities. Res Mechanica, 23 (1988) 97-305.

DISLOCATION SUBSTRUCTURE AND CREEP - OBSERVATIONS

4. S Takeuchi & A S Argon. Steady-state Creep of Single-phase Crystalline Matter at High Temperature. J Materials Science, 11 (1976) 1542-1566.

DISLOCATION SUBSTRUCTURE AND CREEP - MODELLING

5. N M Ghoniem, J R Matthews & R J Amodeo. A Dislocation Model for Creep in Engineering Materials. Res Mechanica 29 (1990) 197-219.

GENERAL RECRYSTALLISATION BEHAVIOUR

6. P Cotterill & P R Mould. Recrystallisation and Grain Growth in Metals. Surrey University Press, London, 1976.

7. Annealing Processes - Recovery, Recrystallisation and Grain Growth. 7th Risø International Symposium on Metallurgy and Materials Science, 1986. Eds N Hansen, D Juul Jensen, T Leffert & B Ralph. Risø National Labs, Roskilde, Denmark.

PARTICLE EFFECTS ON RECRYSTALLISATION AND GRAIN GROWTH

8. Recrystallisation and Grain Growth of Multi-phase and Particle Containing Materials. 1st Risø International Symposium on Metallurgy and Materials Science, 1980. Risø National Labs, Roskilde, Denmark.

GRAIN GROWTH THEORY AND MODELLING

9. H V Atkinson. Theories of Normal Grain Growth in Pure Single Phase Materials. Acta Metall, 36 (1988) 469-491.

DYNAMIC RECRYSTALLISATION

10. T Sakai & J J Jonas. Acta Metall, 32 (1984), 189-209.

GENERAL INTRODUCTION

The objective of these notes is to provide a self-contained introduction to the subject of polygonisation, recovery, dislocation patterning and recrystallisation for students with a physics rather than a metallurgical background. To this end nothing is assumed and the technical terminology is explained as the lectures progress. The minimum background will be some appreciation of the theory of elasticity, an elementary introduction to dislocations and other crystal defects and an understanding of cartesian tensors and differential equations. Wherever possible the lectures use examples from real engineering materials rather than idealised alloy systems and the final objective is to equip the student with the tools to tackle problems to understand microstructural evaluation in relevant engineering alloys and ceramics. The emphasis is on the high temperature operation of structures and the associated annealing and deformation processes. Some time will be given to cold working and irradiation behaviour but these areas are not the main theme of the notes.

The notes are arranged in five lectures. Lecture 1 describes the experimental and microstructural observations of dislocation ordering and recrystallisation and how these have been reconciled in the past empirically and by phenomenological models. Lectures 2 and 3 provide the necessary background to understand dislocation interactions, with one another and with precipitates and solutes, and the evolution of precipitate and cavity populations. Lecture 4 describes how dislocation ordering can be modelled as part of the larger problem of modelling creep and recovery behaviour. Lecture 5 looks at the modelling of primary and secondary recrystallisation processes in complex alloys.

LECTURE 1
EXPERIMENTAL OBSERVATIONS OF DISLOCATION ORDERING AND RECRYSTALLISATION

1.1 INTRODUCTION

The plastic deformation of crystalline materials is accompanied, in all but exceptional cases, by the multiplication of dislocations. The multiplication process is heterogeneous in character and the dislocation population after deformation at low temperatures (<0.3Tm) is non-uniform. Deformation at higher temperatures or annealing of dislocations formed from cold working results in a more ordered dislocation population. This process is referred to as **polygonisation** when a uniform structure is formed but in circumstances dependent on the material the dislocations form planar arrays referred to as **sub-grain boundaries**. The decrease in yield stress produced by annealing, arising from a reduction in dislocation density and the ordering of the remaining dislocations, is referred to as **recovery**.

If the dislocation density is high, annealing at high temperatures sometimes results in a sudden change in structure where a new smaller grain size is formed. The dislocation density within these new grains is low. This process is termed **primary recrystallisation**. Subsequently there is a rapid growth of the new grains and the material strength drops to a minimum. During this process a few grains grow at the expense of the rest; this is known as **secondary recrystallisation** or abnormal grain growth. Subsequently, once a more uniform grain size distribution is obtained 'normal' grain growth proceeds at a slower rate. The terminology defined here is summarised in Transparency 1.1.

The character of the material - the nature of the atomic bonding (metallic, covalent, ionic), the crystal structure, the stacking fault energy, the presence of solutes, the presence and evolution of precipitates, the occurrence of shear (martensitic) transformations - has a strong effect on these dislocation and grain boundary phenomena and their associated macroscopic properties such as creep strength and plastic yield stress. Materials subjected to cyclic stress have dislocation substructures that are dependent on the magnitude of the cycling. These

systems are surprisingly stable.

Having defined some of the terminology let us look at some of the observations of the behaviour of real materials.

1.2 DISLOCATION ORDERING DURING DEFORMATION AND ANNEALING

Plastic deformation is a very heterogeneous process and the micro-structures of cold worked materials reflect this. Dislocations formed at favourable locations (sources) move until blocked, interact with dislocations on other slip systems during the process and eventually form complicated tangles with wild spatial fluctuations in density and local concentrations of dislocations of a particular sign. The degree of disorder depends not only on the character of the material but also on the type of loading and the previous loading history. Temperature can also have effects at surprisingly low temperatures.

The stress-strain curve of a well-annealed pure single crystal of an fcc metal shows three stages of hardening, see Fig 1.1. The first stage, or easy glide, has little hardening and only one slip plane is involved. The dislocations are generated on a few slip bands and are spaced out along these bands as they are generated. Stage II ideally shows linear hardening resulting from the interaction of dislocations on other slip planes. The dislocation distributions become increasingly complex, as the dislocation density increases, with the formation of dislocation dipoles, multipole bundles and, in some cases, cellular structures. In Stage III, the hardening starts to saturate, because of dynamic recovery effects permitted by the high dislocation density and movement of the dislocations off their original glide plane. The dislocation distribution becomes more heterogeneous with regions of very high dislocation density and regions free of dislocations.

In pure polycrystalline materials Stage I is essentially absent and complex dislocation structures are present from the earliest stages of deformation, propagating from interaction at the grain boundaries. Figure 1.2 shows the tangled dislocation structure of cold worked stainless steel.

The character of stress strain curves in other classes of metals and ceramics are different and the presence of solutes or second phases have c profound effects. However the appearance of increasingly complex dislocation structures with deformation is universal and the ability to form low energy dislocation structures increases with temperature. In bcc metals this is conditioned by a high flow stress for the screw components of dislocations and the importance of thermally activated glide. In ionic and covalently bonded materials there is a high flow stress for all dislocations and dislocation re-arrangement is again restricted to high temperatures.

In all materials there are profound changes in the nature of dislocation structures at temperatures where diffusive processes are important (0.3Tm) and edge dislocations can move non-conservatively. Loose cellular structures that form at lower temperatures can be pulled into tighter and more uniform arrays that define sub-grain boundaries. Figures 1.4 to 1.7 show some examples from etch pit and transmission electron micrographs of structures seen in real metals. Such structures can also be formed by recovery of cold worked metals at temperatures below those required for recrystallisation. It is observed, however, that unless the sub-grain boundaries are pinned by precipitates they are mobile and the sub-grain size increases with time. There is also a tendency for the misorientation between sub-grains to increase as the structure coarsens and eventually the sub-grains will produce new grains.

During creep and hot working the sub-grain structure is often stable and characteristic of the load, at least for steady state creep. The misorientation tends to be independent of stress and after a transient independent of strain as well, but characteristic of a particular material, see Fig 1.8. This observation is sometimes taken to indicate that the sub-grains are dynamic features constantly being nucleated and annihilated, rather than persistent structures.

The sub-grain diameter d is found to be inversely related to the load, ie $d \propto 1/\sigma_a^m$ where m is frequently found to be 1 but is often closer to 1.5 in the case of hot working rather than creep. A frequently used relation is:

$$\tau = K\mu b/d \qquad (1.1)$$

where τ is the resolved shear stress = $\sigma_a/2$, μ is the shear modulus, b is the Burgers vector and K is a constant characteristic of the material. Figure 1.9 shows some examples of the relationship for single crystals. Typically K is around 10 for metals but is considerably higher for ionic solids. The dislocation density inside the sub-grains is frequently found to be proportional to $(\tau/\mu b)^2$ and hence from eq (1.1) the sub-grain size is inversely proportional to the square root of the dislocation density. This observation has some significance as we shall see in Lecture 4.

Not all materials show clear sub-grain boundary formation. The presence of large fractions of second phases or alloys with over-sized solutes tend not to inhibit sub-grains, but accumulated dislocation formed uniformly or as debris around inclusions. In fcc metals with low stacking fault energy (eg stainless steels) the sub-grain walls are less well defined (or well knitted) and are sometimes only observed at high strains. This has been interpreted as due to the splitting of dislocations into pairs of partial dislocations interfering with dislocation climb.

1.3 OBSERVATIONS OF RECRYSTALLISATION IN WORK HARDENED ALLOYS

Recrystallisation can be approached by looking at the mechanical properties of an alloy or by looking at the microstructure. We will first of all look at the strength of cold worked materials during annealing.

Most cold worked materials exhibit some degree of recovery on annealing, but in some materials, such as precipitate hardened alloys the recovery can be minimal. Single phase and particularly pure materials can fully recover their softness without recrystallisation, but nearly all work hardened materials will recrystallise if annealed at a high enough temperature. Typical behaviour is shown in Fig 1.10 for isothermal annealing for a fixed period. The difference between recovery and recrystallisation is concerned with timescales and homogeneity. Recovery is a progressive process which occurs more or less uniformly over the material. Recrystallisation is a sudden process leaving the material fully softened, but it occurs locally and macroscopically can appear to be progressive.

The kinetics of recrystallisation of a complex alloy (316 stainless steel) can be seen in Fig 1.11. Typically recovery progresses rapidly then saturates to a value which is insensitive to the temperature, but is dependent on the past history. Recrystallisation occurs after some incubation period, which decreases with increasing temperature. Full softening is also achieved within a shorter period at higher temperatures. Most of the softening effect comes from primary recrystallisation.

Recrystallisation is important in the design of a high temperature structure both from the point of view of the plastic strength and the creep strength. Figure 1.12 shows that in the dislocation creep regime cold work can increase the creep resistance provided the material has not recrystallised. We will investigate how this can happen in Lecture 4.

Turning now to the microstructural observations. The reduction in hardness or strength coincides with the nucleation of a new grain structure inside the old grains. This process is termed primary recrystallisation. It is shown schematically in Fig 1.13. These new grain nuclei are found to grow linearly with time until they impinge on one another. This marks the end of the primary recrystallisation process and determines the new grain size, D_b, see Fig 1.14. The recrystallised grain size is thus:

$$D = G(t-t_o) \qquad (1.2)$$

where t_o is the incubation time and G is a measure of the grain boundary velocity, t_o and G are both functions of temperature. A useful concept is the fraction of material recrystallised, F, which may be used to assess the evolution of the softening. We will investigate the time and temperature dependence of these processes in Lecture 5.

The behaviour of single and multiphased alloys differ in many respects and the recrystallisation behaviour is intimately connected with the evolution of precipitate populations. In particular the incubation time for primary recrystallisation will often be controlled by precipitate coarsening rates. In some cases recrystallisation is nucleated on precipitates. Irradiation is also important in affecting recrystallisation rates. Invariably displacement damage reduces the incubation times. This is

probably due both to an increase in hardening (but it must be remembered that irradiation can soften heavily worked materials) and irradiation induced effects on precipitation-precipitate dissolution and coarsening.

Once the primary recrystallisation phase is over, the new finer grain size is generally found to be unstable. Secondary recrystallisation takes the form of abnormal grain growth where a few grains grow at the expense of others. Figure 1.15 shows an optical micrograph of such abnormal grain growth. Note the curvature of the boundaries adjacent to the shrinking smaller grains. This is the driving force for the process. Secondary recrystallisation continues until the new larger grains impinge on one another. Subsequently grain growth proceeds slowly by normal grain growth. Normal grain growth is a process where the smallest grains in a size distribution disappear leading to an overall increase in size.

Normal grain growth is observed to follow:

$$D^n - D_o^n = ct \qquad (1.3)$$

where c is rate constant which is a function of temperature, D_o is the initial grain size and n lies between 2 and 5. Abnormal grain growth however is found to follow a linear growth law of the same type as (1.2) but of course with different values of G and t. The final grain size is determined by the number of abnormally growing grains. These phenomena are again addressed in Lecture 5.

1.4 RECRYSTALLISATION DURING HOT WORKING AND CREEP

Dynamic recrystallisation is simply recrystallisation that takes place during deformation. It is important as it is a process that reduces the load required for hot working at the high strain rates needed in various manufacturing processes. Dynamic recovery processes, where dislocation density is reduced by mutual interactions during deformation, is better known and better understood. Dynamic recrystallisation involves the continuous or periodic nucleation of new grains during deformation, with their subsequent growth sweeping up dislocations and precipitates, softening the material.

Before discussing dynamic recrystallisation as such, we will look at some associated phenomena. First of all during plastic deformation or creep there is frequently more activity in the regions adjacent to the grain boundaries rather than in the grain interiors. An example is shown in Fig 1.16 where a sub-grain structure is seen to be associated with the grain boundaries. This strain concentration may be associated with local stress concentrations due to inhomogeneity interaction between the grains or it may be because the grain boundaries provide a source of dislocations. In fact some grain boundary sliding observations may be due to deformation adjacent to grain boundaries.

The second observation is that the incubation time for recrystallisation is sensitive to stress. Creep of cold worked material is sometimes accompanied by an increasing creep transient, rather than the usual primary creep seen in annealed material where the creep rate decreases with time, see Fig 1.17. This effect is seen to occur at temperatures below which recrystallisation is normally seen.

Dynamic recrystallisation requires either a high strain rate in hot working or a high stress for creep. The temperature must also be above some threshold. The recrystallisation can occur continuously for high stresses (or strain rates) and the lowest temperatures, or cyclically for lower stresses and higher temperatures.

An intriguing example of cyclic recrystallisation is shown in Fig 1.18, where single crystals and polycrystals of copper are deformed at constant strain rate and high temperature. The single crystal material starts by having a large build-up of stress, until recrystallisation is triggered. When a grain structure is established subsequent stress build-up is lower until the material cycles in a manner comparable to the polycrystal.

In polycrystals there are obviously interactions between the grains that enhance the recrystallisation behaviour. Examples of continuous and cyclic recrystallisation of a steel in the austenitic state are shown in Fig 1.19. This type of behaviour is also seen in ferritic state, in stainless steels and even in ice in glaciers.

Frequently the new grains that drive the dynamic recrystallisation are nucleated at the grain boundaries as a necklace that then propagates inwards as a sequence of necklaces, see Fig 1.20. There is then a coarsening phase that minimises the material strength and then hardening builds up again. At high strain rate there is not time for this coarsening to take place, and as the grain size increases a new grain structure is nucleated. It is this lack of coarsening that inhibits the cyclic behaviour. The development of the grain size with strain is shown in Figure 1.21. For lower strain rates there is an overall grain coarsening with time and several stress peaks, marked as P_i, over the strain range. For the higher strain rates there is overall grain refinement and only an initial stress peak.

1.5 DISLOCATION STRUCTURES DURING CYCLIC LOADING

It might be imagined that fatigue loading would result in very tangled irregular dislocation structures. In fact, cyclic loading produces some complex and persistent patterns that are worth noting.

The range of behaviour can be seen most clearly in pure metals. The cyclic stress-strain curve at low amplitude for copper is shown in Figure 1.22. There are three regions. In region A the cyclic hardening is not saturated and the dislocations are found to form multipolar bundles, often referred to as veins. An example of this is shown in Figure 1.23. In region B the cyclic hardening saturates and is constant over a substantial strain range. In this region the dislocations mainly lie in bands normal to the glide plane. Thin lamellae of slip bands link the thicker bands. The glide plane of the dislocation are parallel to the lamellae. This type of structure is referred to as persistent slip bands (PSB). An example is shown in Figure 1.24, and an idealised schematic structure in Figure 1.25. At high strain ranges, region C, the structure becomes sensitive to the strain range and hardening recommences. The structure becomes tighter with increasing strain range and is characterised by elongated cells, an example is shown in Figure 1.26.

Such structures are seen in bcc and fcc metals at moderate temperature and low strain ranges, which are relevant to many engineering applications.

The scant configuration is dependent on parameters like the material stacking fault energy and the ratio of mobility of screw and edge dislocation components.

Transparency 1.1

Terminology

Dipoles	a stable pair of dislocations
Dislocation bundles	a stable cluster of dislocations of mixed sign
Slip bands	two dimensional arrays of dislocations of finite thickness
Polygonisation	formation of a uniform dislocation network
Dislocation cells	clustering of dislocations into more or less tight walls
Subgrain boundaries	low angle grain boundaries formed by uniform arrays of dislocations
Recovery	reduction of strength by rearrangement and annihilation of dislocation
Primary recrystallisation	reduction of strength by the nucleation of a new smaller grain structure
Secondary recrystallisation	further reduction of strength by 'abnormal' grain growth ie rapid growth of a few grains
Dynamic recrystallisation	continuous recrystallisation during deformation
Normal grain growth	uniform grain growth by the elimination of the smallest grains

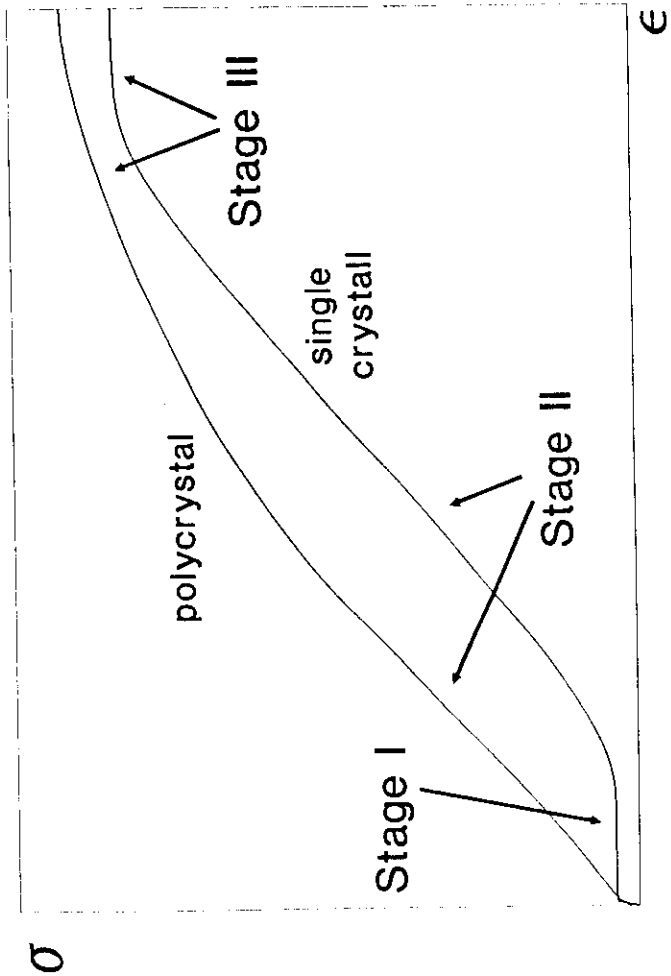

Fig. 1.1 Stress-strain curve for pure fcc metal

Fig 1·2 Dislocation structure of 20% cold worked 316 stainless steel before irradiation

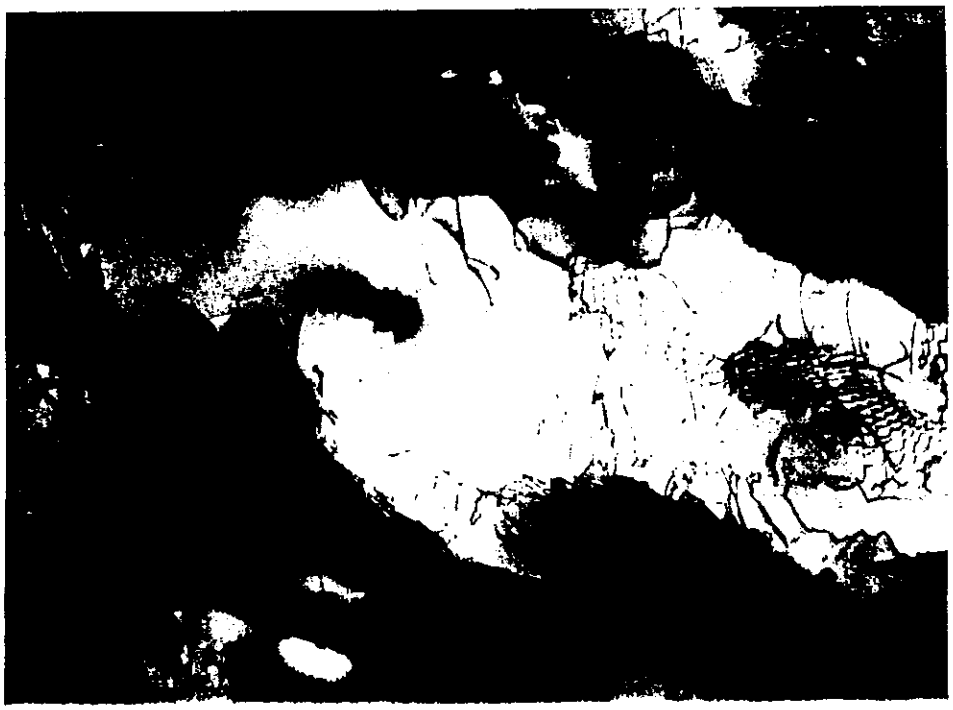

Fig 1·3 Subgrain boundary formation in 20% cold worked 316 stainless steel after 16 dpa in DFR at 580°C

x 250

Figure 1·4 Subgrain boundaries on a cleaved surface of 3C with no visible second phases.

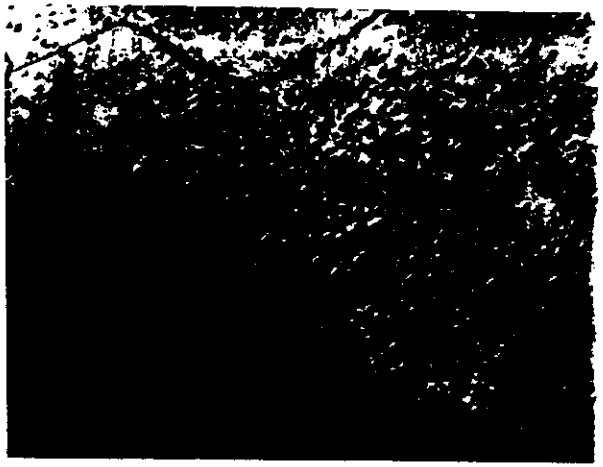

x 125

Figure 1·5 Subgrain boundaries on a polished

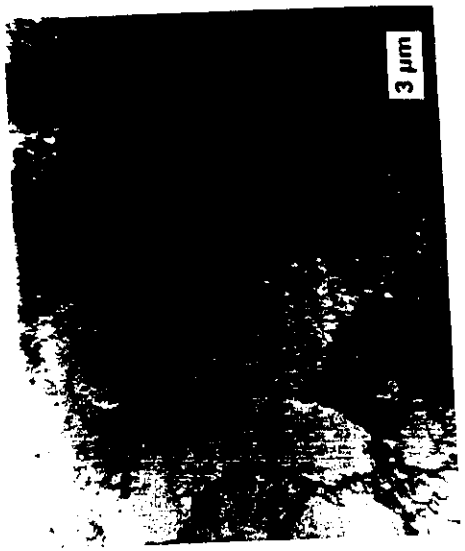

Fig. 1·6a The cell structure showing the relatively random orientation of the cell walls in pure aluminum after a 5% tensile strain.

Fig. 1·6b Tangled dislocations in the cell walls and associated small prismatic dislocation loops in pure aluminium after a 5% tensile strain.

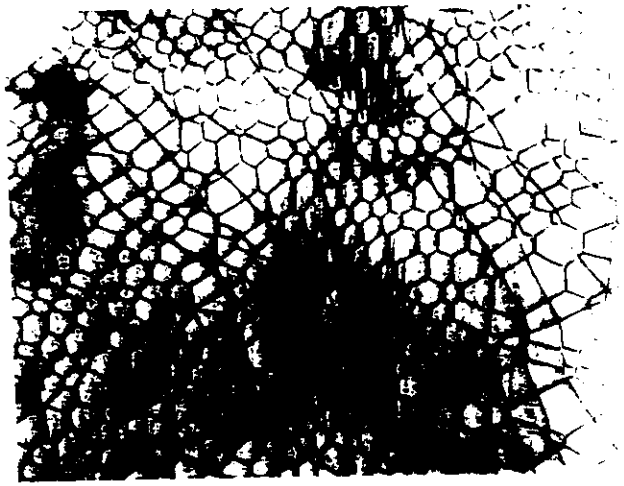

Fig. 1·7a. High voltage electron microscopy survey of dislocation network in the main slip plane of germanium after high temperature compression. (Magnification, 13 200 ×.) Hauser

Fig. 1·7b. Edge dislocation wall crossing screw net after germanium which had been compressed at a high temperature was cooled under a load. (Magnification, 40 000 ×.)

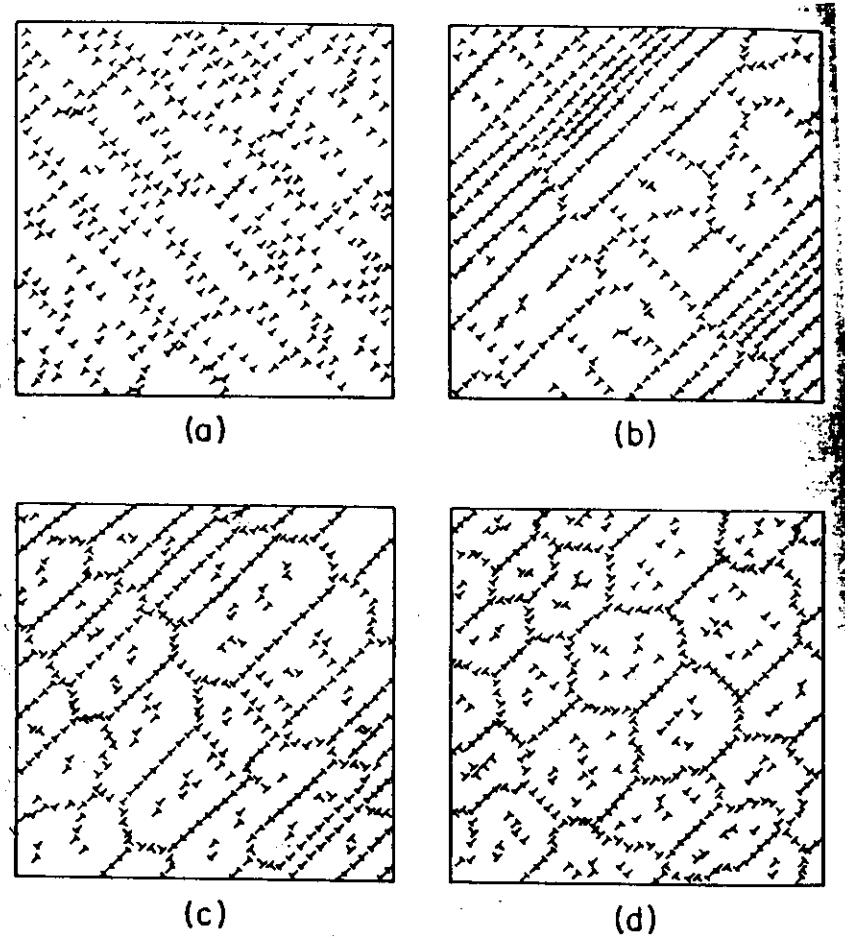

Figure Schematic representation of creep structure in a single crystal at various stages; (a) after instantaneous strain, (b), (c) transient creep, (d) steady-state creep. (Takeuchi and Argon)

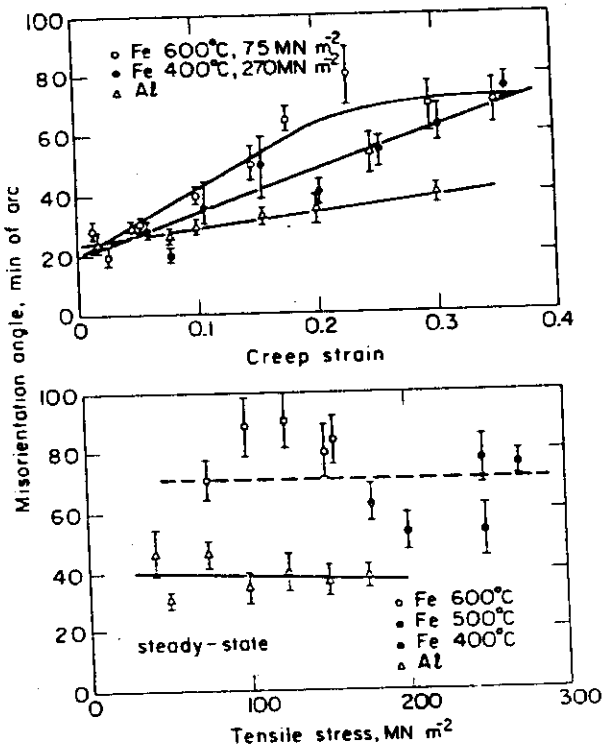

Figure 1·8 Angle of misorientation as a function of creep strain (upper) and of stress (lower) for Al and Fe (Orlova)

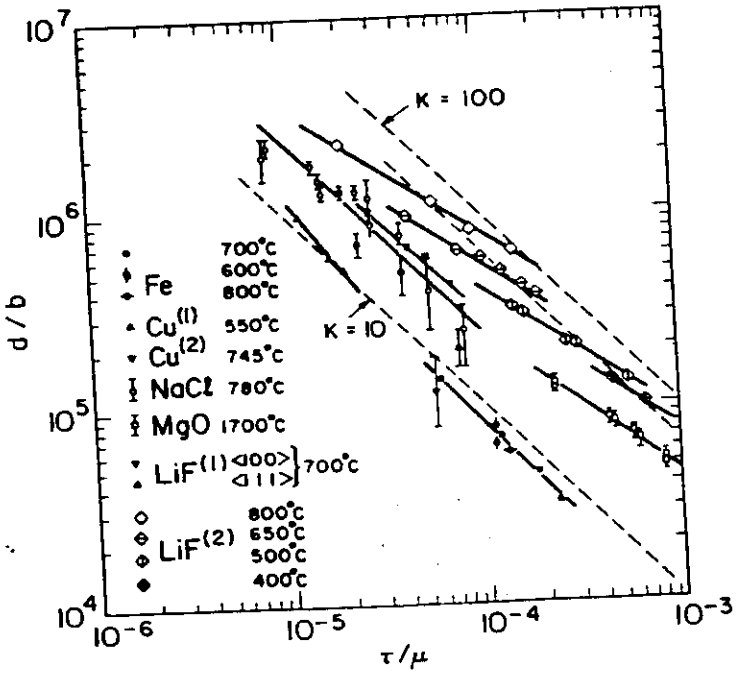

Figure 1·9 Relation between d/b and τ/μ at the steady-state of single crystal specimens of Fe [108], $Cu^{(1)}$ [110], $Cu^{(2)}$ [112], NaCl [115], MgO [116], $LiF^{(1)}$ [118] and $LiF^{(2)}$ [117]. (Takeuchi and Argon)

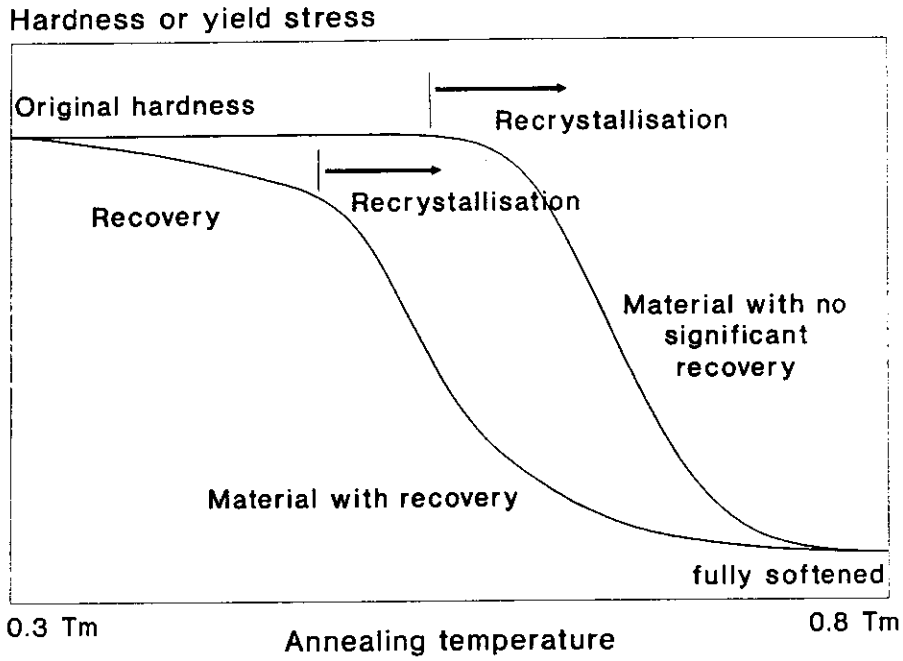

Fig.1.10 Schematic representation of effect fixed time annealing on recovery and recrystallisation.

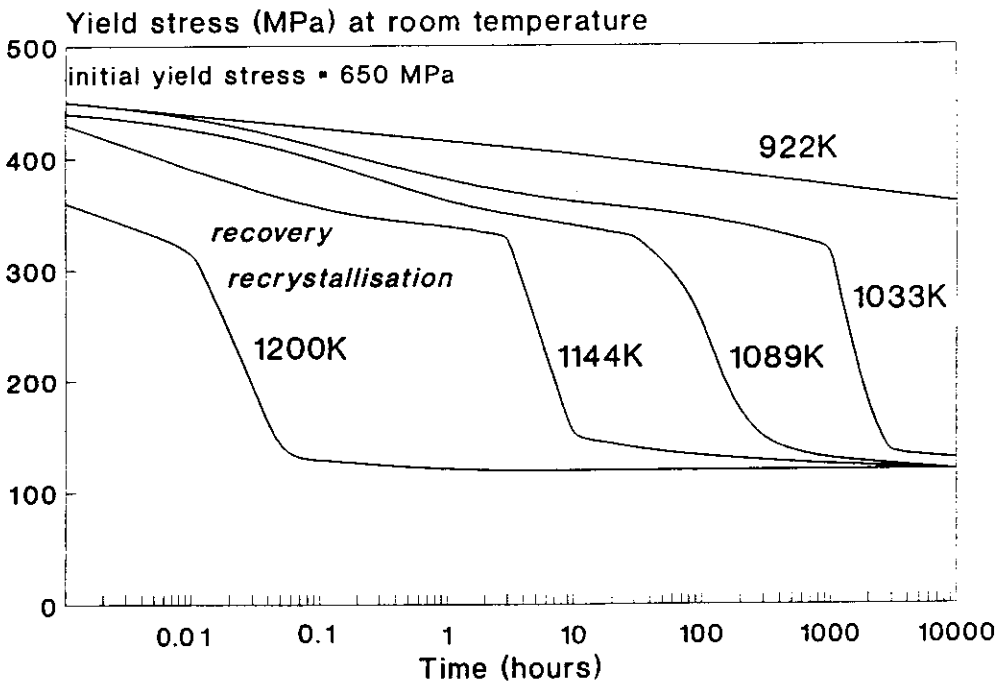

Fig.1.11 Annealing behaviour of 20% cold worked 316 stainless steel (after Paxton and Holmes HEDL-TM-71-126)

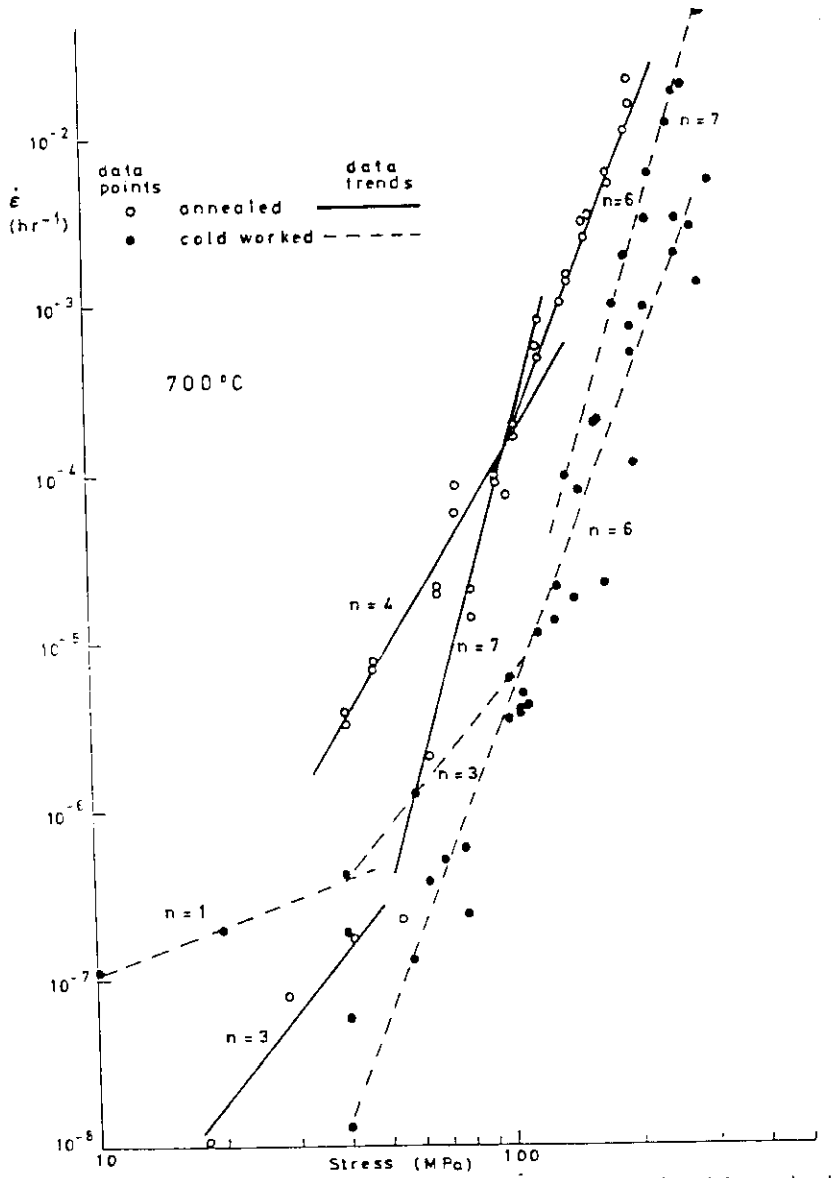

Fig. 1·12 Comparison of the creep behaviour of cold worked and annealed 316 stainless steel

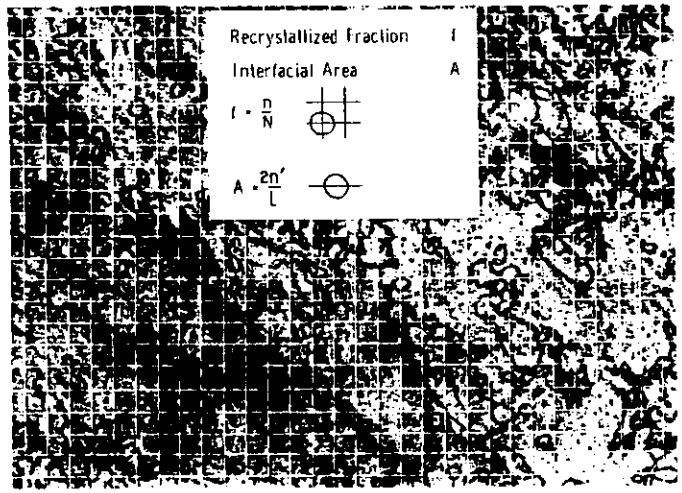

Fig. 1·13 Measurement of recrystallized fraction and interfacial area by quantitative metallography (Speich and Fisher)

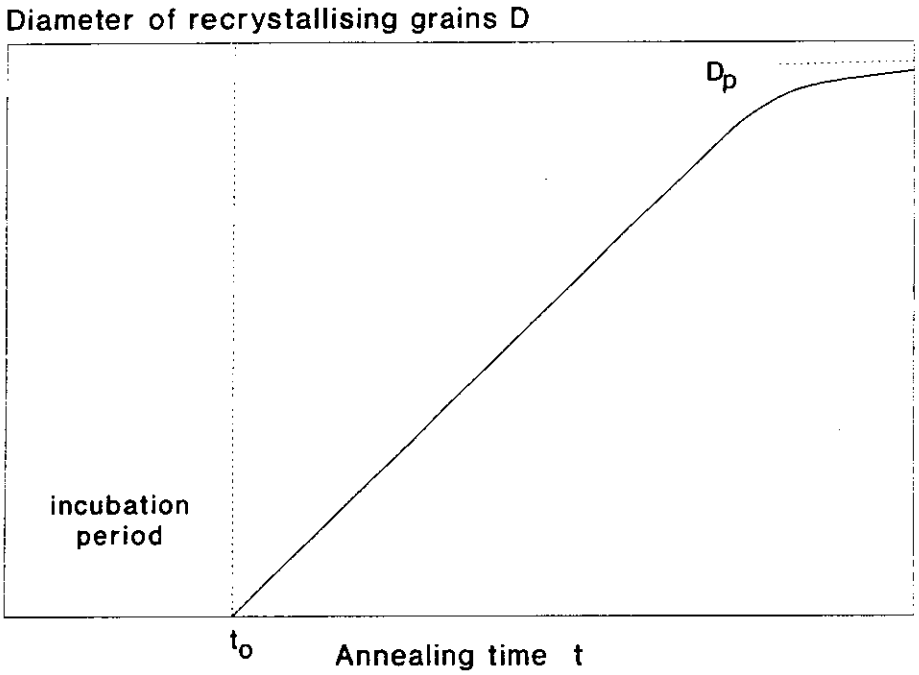

Fig.1.14 Schematic reprentation of renucleation of grains during recrystallisation.

x 2000

Figure 1·16 Subgrain boundary concentration adjacent to a corrugated grain boundary in polycrystalline deformed carbon rich Cu.

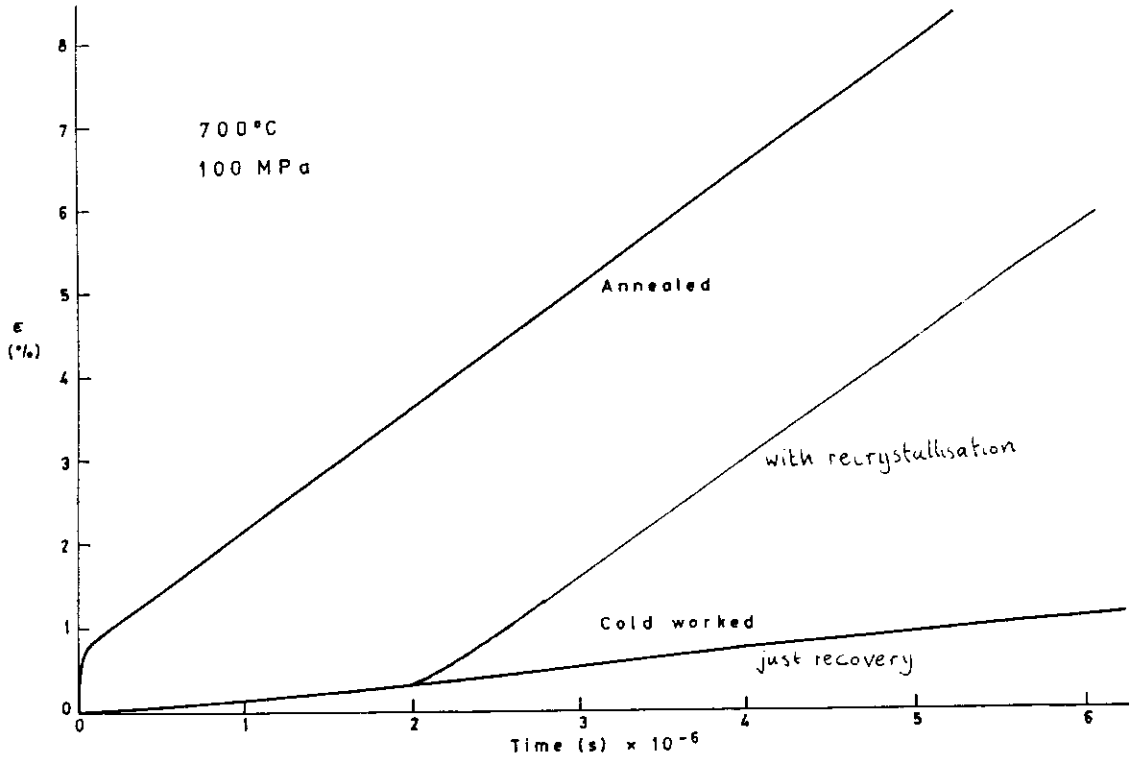

Fig.1·17 Comparison of calculated creep transients for cold worked and annealed 316 steel

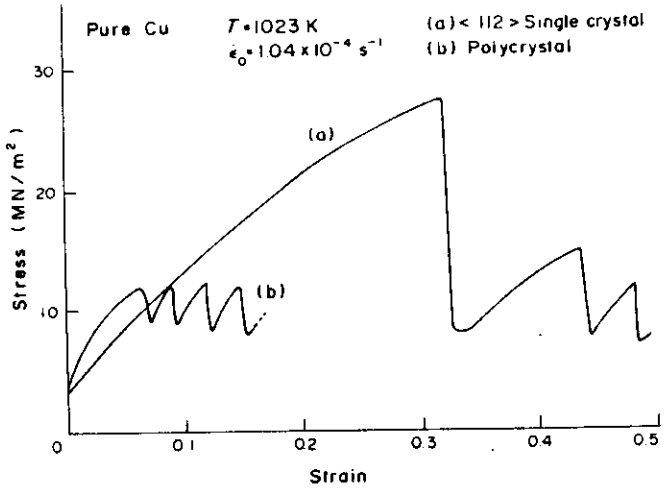

Fig. 1-18 Flow curves for copper deformed in tension (Kikuchi)

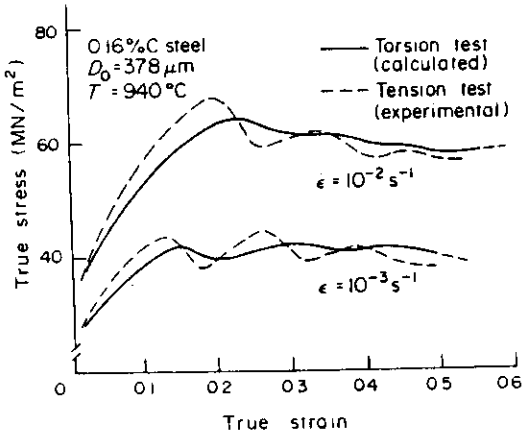

Fig. 1-19 Comparison of *actual* true stress–true strain curves determined in tension with *calculated* torsion curves [30, 31]. The latter were derived from tensile data determined at the strain rate appropriate to each cylindrical "shell" in the simulated torsion bar. The torque contributions of the individual shells were then summed and the effective stress–effective strain curves were deduced by the method of Fields and Backofen [44].

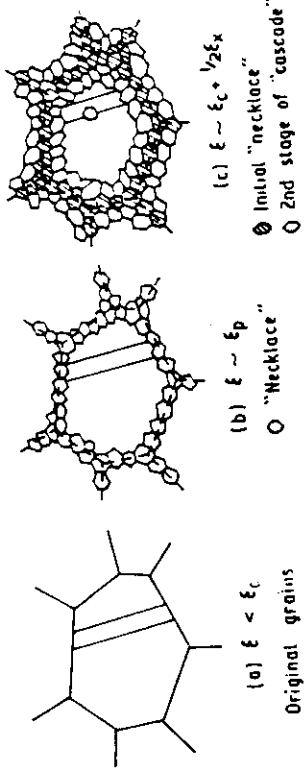

Fig. 1-20 Schematic illustration of the progress of dynamic recrystallisation when the recrystallised grain size is much smaller than the original grain size. (Sellars)

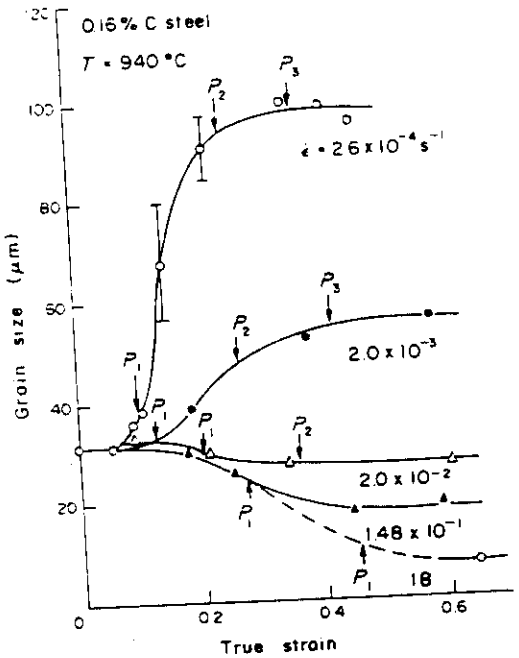

Fig. 1·21 Effect of strain and strain rate on the mean grain size of a 0.16% C steel deformed in tension at 940°C. P_i identifies the strain at the ith flow stress peak. Note that *multiple peaks* are observed during grain *coarsening* (and when grain refinement produces less than a 2:1 reduction in grain size). Conversely, a *single peak* is observed when the grain *refinement* ratio is about 2:1 [29, 31].

(Sakai)

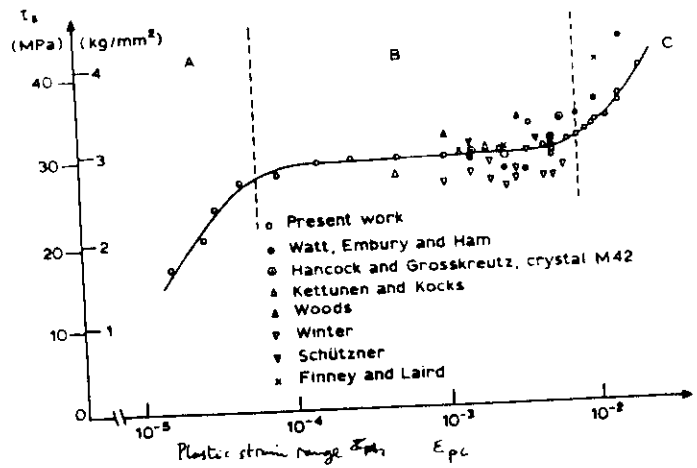

Fig. 1·22 Cyclic stress–strain curve

Fig. I.23 Three-dimensional view of loop patches corresponding to region A of the cyclic stress–strain curve (plastic shear strain amplitude, 2.6×10^{-5}; shear stress $\tau = 19.8$ MPa; region A). (Mughrabi)

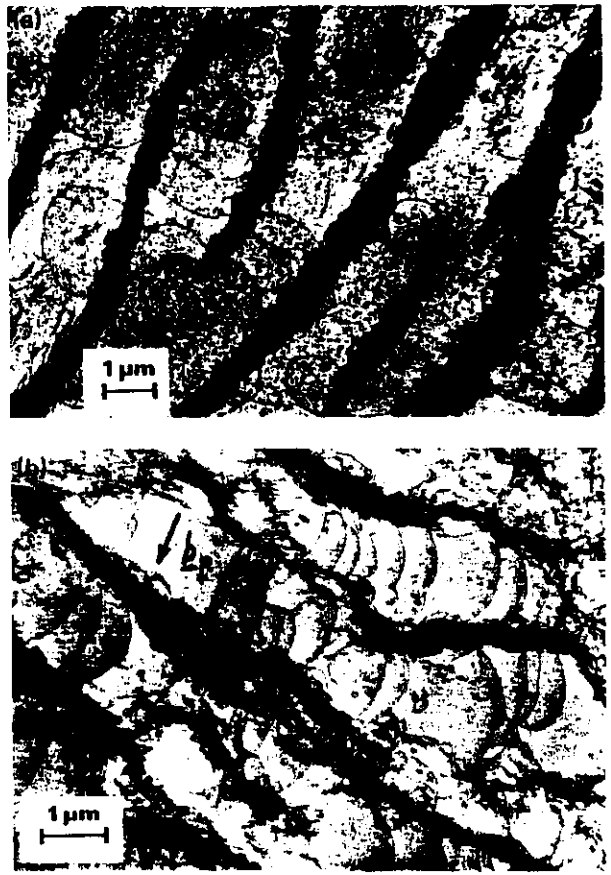

Fig. I.24 Dislocation arrangements in a PSB in a fatigued copper single crystal (stress applied state and neutron irradiated; section parallel to the primary glide plane). ((a) From ref. 25; (b) from ref. 24.) (Mughrabi)

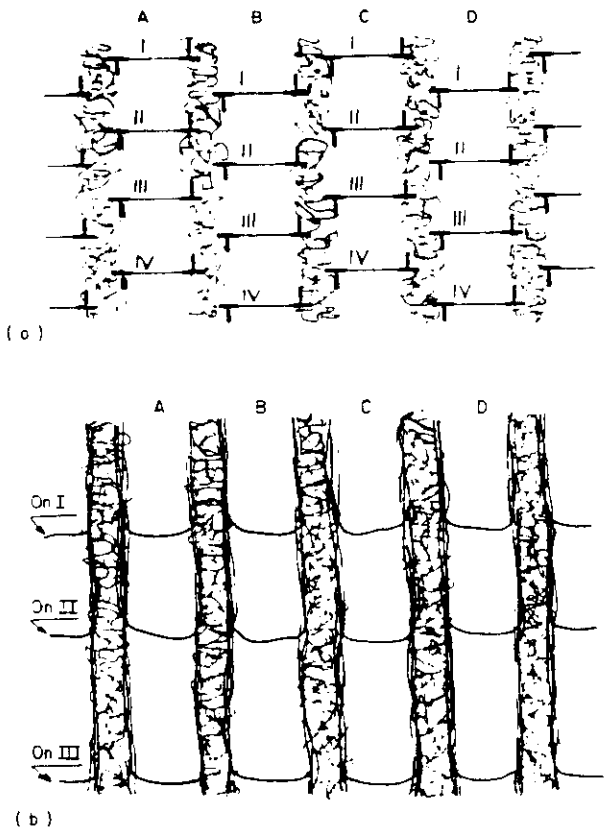

Fig. 1.25 (a) Idealized schematic representation of the entrapped dislocation debris and dipolar structure within a PSB, in a view parallel to [1$\bar{2}$1], showing how the dislocation slip planes are staggered so as to achieve the dipolar tilt wall arrangement (the wall width is exaggerated); (b) schematic view of screw dislocations advancing in coordination along the channels of a PSB, viewed from normal to the primary glide plane (compared with the width of the channels, the displacement of the dislocations is exaggerated). The groups of screw dislocations are labeled to indicate their stacking as seen in (a).
(Mughrabi)

Fig. 1.26 Cell structures observed in three dimensions in a copper single crystal saturated at a plastic shear strain amplitude of 1.45×10^{-2} (region C; dislocation structures neutron pinned in the unloaded state).
(Mughabi)

LECTURE 2

DISLOCATION INTERACTIONS

2.1 INTRODUCTION

This lecture provides the background necessary to understand Lecture 4 on the modelling of dislocation structures during recovery and deformation. This background is essentially in two parts: the forces between dislocations that drive movements to lower energy configurations; and the mobility of dislocations that permit the configurations to be attained. The mobility is partly determined by the intrinsic mobility of the dislocations due to the crystal symmetry and atomic cohesion and partly by interactions with the solutes and precipitates present in any real engineering alloy.

2.2 DISLOCATION-DISLOCATION FORCES

The energy of dislocations is made up of an elastic contribution, which results from a long range elastic strain field and a contribution from the effects of atomic cohesion in the vicinity of the core, which results from a breaking of the local crystal symmetry. Solutions for the elastic field for arbitrarily shaped dislocation loops are extremely complicated for all but the simplest cases. It is possible to calculate the stresses and strains using a Green's function technique and integrating over the dislocation length (see Micromechanics of Defects in Solids by T Mura, 1987, for a description of the method), but for the purpose of these lectures we can make do with solutions for straight infinite dislocations in an isotopic elastic continuum.

The dislocation is characterised by its Burgers vector. A dislocation with a Burgers vector parallel to the dislocation line is known as a pure screw dislocation and a dislocation with a Burgers vector normal to the dislocation line is known as a pure edge dislocation. Dislocations with Burgers vectors arbitrarily oriented to the dislocation line are referred to as mixed dislocations. The stress field for our long straight dislocation is described generally in cylindrical co-ordinates by:

$$\sigma_{ij} = \mu b\, f_{ij}(\theta)/2\pi r, \qquad (2.1)$$

where μ is the shear modulus, b is the magnitude of the Burgers vector, r the distance from the dislocation and $f_{ij}(\theta)$ is a function dependent on the relationship between the Burgers vector and the dislocation line (see Fig 2.1).

The stress field around a pure screw dislocation is isotropic and shear in character, ie:

$$f_{r\theta}(\theta) = f_{\theta z}(\theta) = 1, \qquad (2.2)$$

all other components are zero.

The stress field around a pure edge dislocation consists of dilatation and compressive parts below and above the dislocation line (see Fig 2.2). The stress components are:

$$f_{rr} = (\theta) = f_{\theta\theta}(\theta) = -\sin\theta/(1-\nu),$$

$$f_{r\theta}(\theta) = \cos\theta/(1-\nu),\ f_{zz}(\theta) = -2\nu\sin\theta/(1-\nu) \text{ and}$$
$$f_{r\theta} = -f_{\theta z} = 0 \qquad (2.3)$$

where ν is Poissons ratio for the material.

The self elastic energy of a dislocation is complicated by the stress singularity at the core. We assume the core energy is small and a cut-off is made at a distance of 1 atomic spacing. The elastic energy per unit length of dislocation is approximately:

$$E_d = (\mu b^2/4\pi K_1)\ln(R/a) \qquad (2.4)$$

where R is the dimension of the body containing the dislocation and $K_1 = 1$ for pure shear dislocations and $K_1 = (1-\nu)$ for edge dislocations. As R is a variable and the logarithmic term is not particularly sensitive to the value of R/a, $\ln(R/a)$ is frequently taken as 4π:

$$E_d = \mu b^2/K_1 \qquad (2.5)$$

The self energy of dislocations is large and because of this dislocations are thermodynamically unstable as the configurational entropy is too small to provide an offset. The dependence of the dislocation energy on the square of the Burgers vector means that dislocations usually have Burgers vectors corresponding to the smallest lattice vectors, ie in the close parked directions. Occasionally dislocations are formed with other lattice vectors, from reactions between dislocations or from point defect clustering and in some materials several types of stable dislocations are found.

There are two types of force that must be considered when determining equilibrium dislocation configurations: forces that arise from interactions with elastic fields (applied or from other dislocations and other

parts of the same dislocation if it is not straight), and forces from the curvature of the dislocation line-line extension. We will just consider the elastic field interaction for the time being.

The elastic force acting on a dislocation can be derived by looking at the elastic work done on moving the dislocation. If we imagine a dislocation moving in its glide plane in response to an applied shear stress τ_a acting in the glide plane then the work per unit length done in moving the dislocation a distance dx in the glide plane is $dW = b\tau_a dx$. The force per unit length of dislocations is thus $F = b\tau_a$. This can be generalised as the Peach-Koehler formula:

$$F = \underline{b}.\underline{s} \times \underline{l} \qquad (2.6)$$

where $\underline{l}$ is the vector lying along the dislocation line and s is the deviatoric stress tensor ($\underline{s} = \underline{\sigma} - {}^1/3\ \underline{I}$ trace $\underline{\sigma}$. The deviatoric stress is used rather than ordinary stress as dislocations do not interact directly with hydrostatic stress.

As we shall see dislocation motion is of two types: (i) conservative (glide); and (ii) non-conservative climb. To investigate dislocation

motion we need to resolve the force into the components that act on these two types of motion. Glide is determined by the force resolved into the slip plane:

$$F_g = \underline{b}.\underline{s}.\underline{n} \qquad (2.7)$$

where n is the normal to the slip plane. Climb is determined by the force resolved into the direction normal to the dislocation and slip plane:

$$F_c = -\underline{l}.\ (\underline{n} \times \underline{s}.\underline{b}) \qquad (2.8)$$

For a pure edge dislocation (2.8) becomes:

$$F_c = -\underline{b}.\underline{s}.\underline{b}/|\underline{b}| \qquad (2.9)$$

Transparency 2.1 gives the mutual forces between parallel dislocations. This enables us to determine the equilibrium configuration of dislocation dipoles. Let us first consider screw dislocations of opposite sign.

In this case the interaction is always attractive. If the motion of the dislocation is restricted to a single glide plane, then the dislocations will move together along the glide plane until they are at minimum separation, see Figure 2.3.a. Screw dislocations of the same sign are always repulsive and there is no equilibrium separation. A large population of screw dislocations of mixed signs will tend to clump into bundles (veins). A large population of the same sign will tend toseparate so as to maximise the distance between individuals.

The behaviour of edge dislocations is more complex. For dislocations of opposite sign the interaction is attractive when the dislocations are side by side, but repulsive when the dislocations are one above the other. If the motion of the dislocation is constrained to the glide plane, the dislocations are attracted to form a staggered dipole, see Figure 2.3.b. When the dislocations have the same sign the reverse is true; the dislocations are attracted when one above the other and repelled when side by side. If the dislocations are within the attractive region they will form a dipole with one vertically above the other, see Figure 2.3.c. If

outside the zone of attraction they will repel one another. As we shall see in Lecture 4, the behaviour of large populations of edge dislocations of mixed sign is complicated. Dislocations of the same sign however, have a particular configuration with low energy - the tilt boundary, which is formed by a wall of edge dislocations one above the other. This configuration can only form properly when some degree of dislocation climb is permitted, as the base energy is lowest when the dislocation spacing is regular.

Transparency 2.2 gives the interactions between straight parallel dislocations when they have different Burgers vectors. Dislocations of orthogonal sign are generally attractive, and form stepped dipoles that can continue to move together by glide, unlike dislocations with the same Burgers vector but opposite sign. Pairs of such dislocations can lock together and become immobile until unlocked by a dislocation of opposite sign or by a local stray concentration. In fcc metals such barriers are known as Cottrell-Lomer barriers, and are particularly sessile as the dislocations interact in such a way as to split into particles with stacking faults that prevent motion. In some systems the locked dislocations form a dislocation with a new Burgers vector that can be mobile with a glide stress higher than usual.

2.3 DISLOCATION CLIMB AND GLIDE MOBILITY

Dislocations have two main types of motion: glide which is the propagation of slip through the crystal lattice with only local atomic rearrangement at the dislocation core as the dislocations move; and non-conservative motion or climb which requires the absorption or emission of point defects by the dislocations as they move. Pure screw dislocations only move by glide, and a number of glide planes within the slip system are generally available for the glide. Edge dislocations are constrained to a single glide plane and have to climb to move off it.

A glide loop is a dislocation loop lying on a single glide plane, see Figure 2.6a. Inevitably, it will have have parts which are edge in character and parts which are screw in character. Unless the dislocation is rectangular, most of the loop will consist of mixed dislocations. Under the action of a shear stress the loop will expand or contract in such a manner as to relax the stress. This glide will start when the shear stress exceeds a threshold stress, the glide or flow stress of the dislocations. This stress can be quite different for screw

and edge components. If the dislocation meets some obstacle, a pure dislocation can cross-slip onto a new glide plane, see Figure 2.6b, but an edge dislocation has to climb.

The flow stress for dislocations is dependent on the nature of the atomic bonding and the crystal symmetry. When it is dependent only on the stress required to push the dislocation one atomic spacing, it is known as the Peierls-Nabarro stress, and can be estimated from simple atomic models. The intrinsic flow stress in pure fcc metal is very small, of the order the stress being rather larger for a screw dislocation than an edge one. In fcc metals with a low stacking fault energy (copper, stainless steel etc) the dislocations can split into partials with smaller Burgers vectors. Not only does this reduce the energy of the dislocation, but it also significantly reduces the flow stress. Metals with bcc structures are important for many engineering applications, and this class of metals show a strong temperature dependence of yield point, which is not seen in fcc metals. It is frequently observed that a high proportion of dislocations have a flow stress not too different from fcc metals, but the core structure of the screw component is split in a manner to impede glide. The screw dislocations have to move by nucleating kinks (steps into the glide plane on the dislocations). Dislocation glide then proceeds by motion of the kinks along the dislocation. The apparent glide stress and the dislocation mobility is controlled by the energy to form a kink. The same is true for covalent crystals, where the extreme nature of the bonding forces dislocations to lie closely to particular crystal axes. Ionic crystals also have a large flow stress, typically $10^{-2}\mu$, which again results in a tendency to the flow being thermally activated and the dislocation mobility sensitive to temperature. Dislocation glide mobilities in pure metals are reviewed in Transparency 2,3.

In practice, linear mobility laws are found to break down as a series of power laws (Gilman) where the power changes according to the stress range. Another way of looking at it is to have a threshold stress for dislocation motion τ_c and an upper limit to dislocation velocity determined by the shear wave velocity v_s:

$$v_g = M_g b\,(\tau_g-\tau_c)/[(1+M_g b(\tau_g-\tau_c)/v_s] \qquad (2.10)$$

Cross slip often requires a local stress which is greater than that for primary slip, and is usually a thermally activated process in fcc metals, where primary slip is easy. The reason for this is that in fcc metals the screw dislocations are dissociated into partials which have edge components. For cross slip to occur the partial dislocations have to be pinched together locally. In all systems cross slip has to be nucleated by a segment of screw dislocation sufficiently long to overcome the line tension as the cross slip segment bows out onto the cross slip plane.

Dislocation climb proceeds by the emission or absorption of vacancies or interstitials. Interstitials are not usually thermal defects. They are important in radiation damage as they are produced in large quantities as Frenkel pairs, with vacancies as part of the displacement damage process. They can be produced under certain circumstances during dislocation climb at high stress levels. Vacancies are thermal defects, and are present with concentrations that increase with temperature. At temperatures above 0.3Tm there is a significant exchange of vacancies, with dislocations causing local random climb events.

The understanding of dislocation climb relies on a similar process to kink propagation, but in this case the step on the dislocation is out of the glide plane and is known as a jog, see Figure 2.7. There are essentially two regimes for dislocation climb:

(i) where the climb is hindered by jog concentration, and
(ii)where climb is limited by sources and sinks of vacancies.

The dislocation climb mobility under these regimes is summarised in Transparency 2.4.

After hardening is established, dislocation motion is more likely to be determined by interactions with other dislocations. Dislocations that are inclined with some component parallel to the dislocation under consideration will modify the force seen by the dislocations, because of their electric fields. Dislocations that are inclined with some component normal to the dislocations under consideration will provide obstacles that have to be cut. These are often referred to as trees or forest dislocations. A dislocation moving through a forest of other dislocations will bow outwards, increasing the

force at the point of contact, see Figure 2.8. During the cutting process a jog is formed at each dislocation at the point of contact. In the case of intersecting screw dislocations, the jogs formed have edge character and in order for further glide to occur, the jog has to climb, as it is dragged along. Transparency 2.5 gives the mobilities in these cases.

2.4 DISLOCATION SOLUTE INTERACTIONS

In most engineering alloys, oversized solutes are added to increase the strength, and these dominate the mobility of dislocations. Solutes can affect dislocations in a number of ways. Stationary dislocations can attract an 'atmosphere' of solute atoms that arises because of the elastic interaction between the mismatch field of the solute atom and the dislocation strain field. It is only with the edge components of dislocations that this interaction is significant. This atmosphere is referred to as the Cottrell atmosphere.

The motion of dislocations with an atmosphere will be controlled by the rate of diffusion of the atmosphere as the dislocation drags it along. There will however be a stress above which the dislocation can break away from the atmosphere and will then move much more rapidly, see Figure 2.9. This type of behaviour is thought to underly the Portevin-le Chatelier effect. Solutes that are trapped at dislocation cores will have a profound effect on their motion, and when saturated effectively render the dislocation immobile. Both types of solute effect are important in determining recovery and crystallisation behaviour. These effects are quantified in Transparency 2.6.

2.5 DISLOCATION-PRECIPITATE INTERACTIONS

Precipitates and inclusions of various types are used to provide high temperature strength to alloys, and they also are important in determining the recovery and recrystallisation of work hardened alloys. There are two main possibilities in the interactions. The dislocations can bow out between the precipitates until they meet the other side and then move away, leaving loops behind; this is known as the Orowan mechanism, see Figure 2.10. Alternatively, if the precipitates are coherent or soft enough, the dislocations can cut through them. In either case, the mechanism of moving through the precipitate population will be controlled by the volume fraction of the precipitates and the spacing between the precipitates. Transparency 2.7 shows some of the main features.

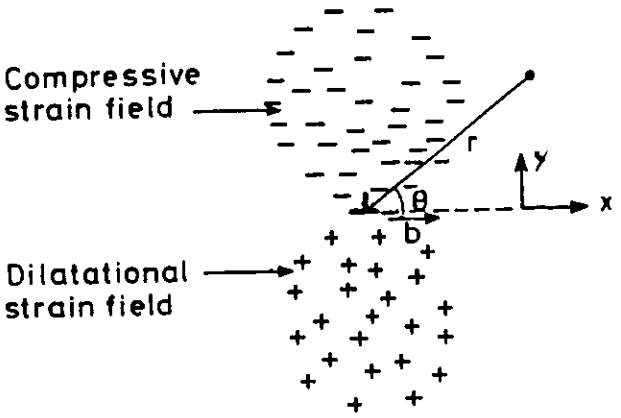

Fig. 2.1 and 2.2 Dislocation co-ordinate system and edge dislocation strain field.

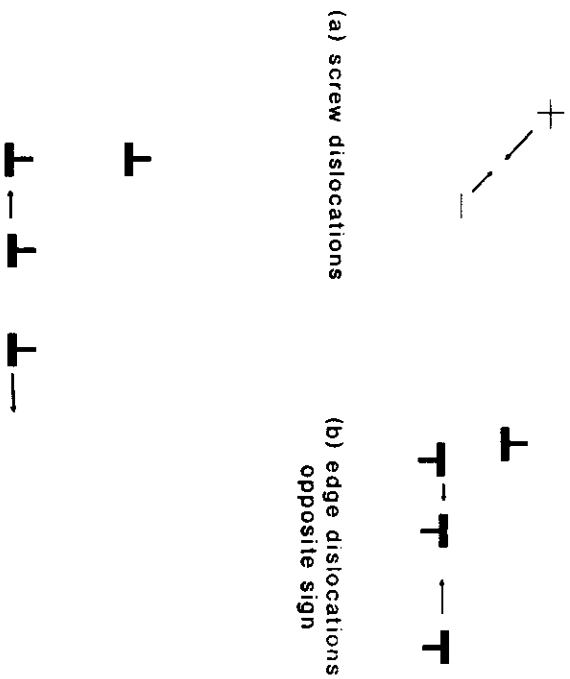

Fig. 2.3 Dislocation dipole reactions.

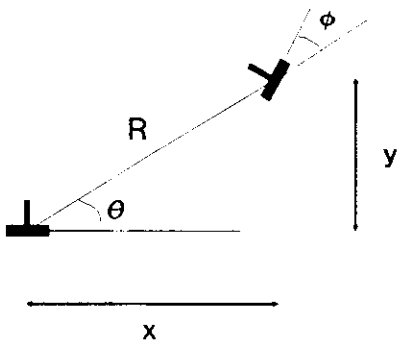

Fig.2.4 Interaction between two parallel edge dislocations.

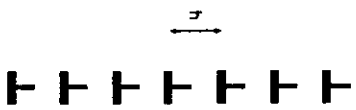

Fig.2.5 Schematic diagram of a tilt sub-grain boundary.

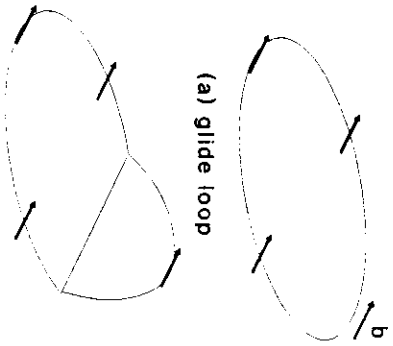

Fig.2.6 Schematic diagram of glide loop expansion

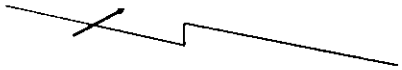

Fig 2.7 Edge dislocation with jog.

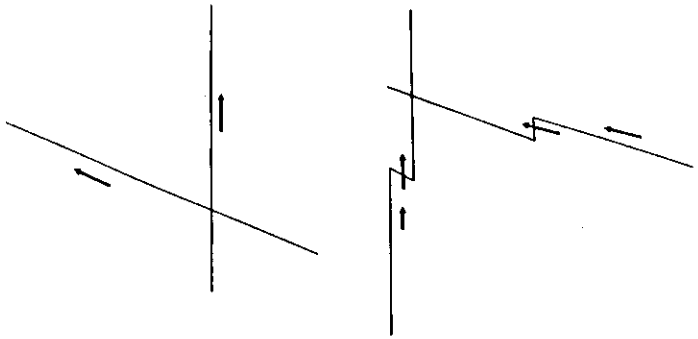

Fig.2.8 Crossing of screw dislocations edge jogs.

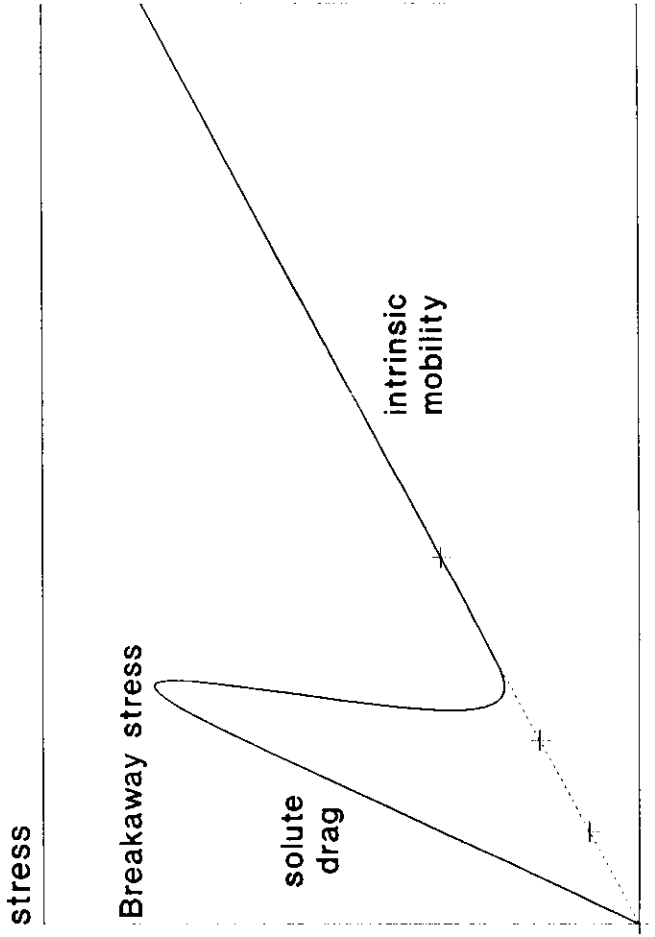

Fig. 2.9 Mobility of dislocations with a solute atmosphere.

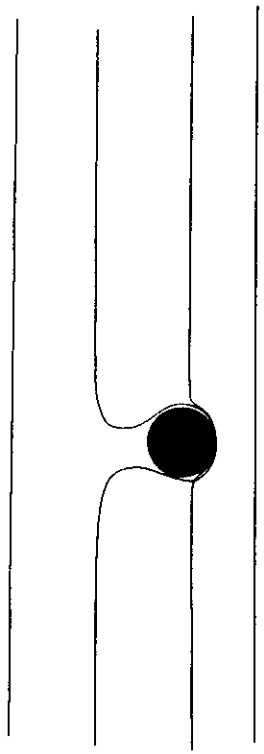

Fig. 2.10 Schematic diagram of dislocations bypassing a spherical particle by the Orowan process.

Force between parallel straight dislocations, with same Burgers vector.

The force between pure screw dislocations is radial:

$$F_r = \frac{-\mu b_1 b_2}{2\pi r} = \frac{-\mu b_1 b_2}{2\pi (x^2+y^2)^{1/2}}$$

The force is repulsive if b_1 and b_2 are of the same sign and attractive if they are of opposite sign.

If both dislocations have the same glide plane the force to glide is:

$$F_g = F_r \cos\theta = \frac{-\mu b_1 b_2 x}{(x^2+y^2)} .$$

The force between edge dislocations is more complex.

There is a radial force:

$$F_r = \frac{-\mu b_1 b_2}{2\pi(1-\upsilon)r}$$

and a tangential force

$$F_\theta = F_r \sin 2\theta .$$

The force to glide is:

$$F_g = F_r \cos\theta + F_\theta \sin\theta = \frac{-\mu b_1 b_2}{2\pi(1-\upsilon)} \frac{x(x^2-y^2)}{(x^2+y^2)^2}$$

The force to climb is

$$F_c = F_r \sin\theta - F_\theta \cos\theta = \frac{-\mu b_1 b_2 y}{2\pi(1-\upsilon)} \frac{(y^2+3x^2)}{(x^2+y^2)^2} .$$

TRANSPARENCY 2.2

Force between parallel straight dislocations with different Burgers vectors

A more general expression for the force between parallel straight dislocations has the following components:

Glide

$$F_g = \frac{\mu |b_a||b_b|}{2\pi(1-\nu)} \quad \frac{\cos\theta \cos 2\phi}{R}$$

Climb

$$F_c = \frac{\mu |b_a||b_b|}{2\pi(1-\nu)} \quad \frac{\sin\theta - \sin(2\phi)\cos\theta}{R}$$

The configurations are shown in Figure 2.4.

For the particular case of $\phi = \theta$ the equation reduces to those in Transparency 2.1.

For the particular case of $\phi = \pi/2 - \theta$, i.e. when the dislocations have orthogonal Burgers vectors, then:

Glide

$$F_g = \frac{\mu |b_a||b_b|}{2\pi(1-\nu)} \quad \frac{x(x^2 - y^2)}{(x^2 + y^2)^2}$$

Climb

$$F_g = \mu |b_a||b_b| \; y \; \frac{(y^2 - x^2)}{(x^2 + y^2)^2}$$

TRANSPARENCY 2.3

Dislocation Mobility in Pure Metals

For many purposes dislocation velocity can be expressed as:

$$v_g = M_g F_g = M_g b \, \tau_g$$

where M_g is the dislocation glide mobility and F_g and τ_g are the force per unit length and shear stress resolved onto the glide plane. Activated dislocation motion against lattice friction (Peierls-Nabarro stress) can be expressed as:

$$v_g = \nu_o b \exp(-\Delta G_o/kT) \sinh(V_g \tau_g/kT)$$

$$M_g \sim \nu_d V_g \exp(-\Delta G_o/kT)/kT$$

where ν_d is the dislocation vibrational frequency, $\bar{V}_g$ is the mean activation volume and ΔG_o the free energy to overcome the lattice friction barrier. When the glide is controlled by propagation of kinks:

$$M_g = 2h^2 a \, \nu_d \exp(-H_{km}/kT) \exp(-\Delta G_{kf}/kT)/kT$$

where h is the kink height of the order of a (the atomic spacing) or b, H_{km} is the enthalpy of kink migration (~10k to 100k) and ΔG_{kf} is the free energy of kink formation (~100k to 10^3k). These energies are much larger in covalently bonded materials.

TRANSPARENCY 2.4

Dislocation Climb

An upper limit to dislocation climb velocity is given by:

$$v_c = M_c F_c = M_c b \tau_c$$

where

$$M_c = D_L b/kT$$

D_L being the lattice self diffusion coefficient.

If jog concentration limits the climb rate:

$$M_c = D_L b^2 C_j/kT$$

where C_j is the jog concentration which, if controlled by thermal fluctuation forms jog pairs:

$$C_j \sim \exp(-\Delta G_{jf}/kT)/b,$$

ΔG_{jf} is the jog formation free energy which is typically of the order $\mu\Omega/15 \sim 5\times10^{3}k$ to $10^{4}k$

For fcc metals with low stacking fault energy, the splitting of the dislocations lead to geometrical factors that have to be taken into account. Argon and Moffat have suggested:

$$M_c = 10^{3} D_L b^2 C_j (\Gamma/\mu b)^2/kT$$

where Γ is the stacking fault energy.

When the climb rate is limited by sources and sink of vacancies, then:

$$M_c = 2\pi D_L b/[(kT \ln(R/\lambda)]$$

or for dislocation pipe diffusions

$$M_c = 2\pi D_p b^3/(kT \lambda^2)$$

where λ is the vacancy path length $(\sim 1/\rho^{1/2})$, D_p is the dislocation pipe diffusion coefficient, and R is the dislocation core effective radius.

TRANSPARENCY 2.5

Dislocation Mobility limited by Forest Cutting and Jog Drag

The velocity of a dislocation impeded by forest dislocations of spacing λ is given by:

$$v_g = v_d \lambda \sinh(\tau_g b^2 \lambda/2kT) \exp(-\Delta G_{jf}/kT)$$

For low stresses the mobility is:

$$M_g = v_d \lambda^2 b \exp(-\Delta G_{jf}/kT)/2kT$$

Jogged screw dislocations drag the jogs along, which limits their mobility. If the jog spacing is L the dislocation velocity is:

$$v_g = D_L \sinh(\tau_g b^2 L/kT)/b$$

and for low stresses the mobility is:

$$M_g = D_L L/kT$$

TRANSPARENCY 2.6

Dislocation-Solute Interactions

The mobility when dragging a Cottrell atmosphere is:

$$M_g = D_a\ kT/[c_a\beta^2\ \ell n\ (R_o/R_i)]$$

where D_a is the solute diffusion coefficient, c_a is the solute average volume concentration, R_o is the outer cut off radius which is of the order $1/\rho^{\frac{1}{2}}$ and R_i is the inner cut off radius which is the greater of the dislocation core radius or β/kT and β is a measure of the mismatch:

$$\beta = (\mu\ b/3\pi)[(1 + \nu)/(1 - \nu)]\ (\Omega_s - \Omega_a)$$

where Ω_s is the solute effective volume and Ω_a the crystal atomic volume.

The dislocation will break free from the atmosphere when $\tau_g \geq 17\ c_a\ \beta/b$. The residual friction stress is of the order $\pi\ C_o\ \beta/b$.

In some cases solutes are trapped at the dislocation core and the dislocation velocity is given by:

$$v_g = 2\ b\ \nu_d\ \exp\ (-H_{am}/kT)\ \sinh\ (\tau_g\ b^2L_a/kT)$$

where H_{am} is the activation enthalpy for core diffusion of the solute and L_a is the spacing of the solute atoms along the dislocation. Dislocation breakaway from core solute atoms will occur when $\tau_g \geq \mu\ (\Omega_s - \Omega_a)/L_a\Omega_a$, which for saturated dislocation cores is a very large stress.

TRANSPARENCY 2.7

Dislocation-Precipitate Interactions

For small volume fraction the Orowan stress to pass through a population of incoherent precipitates is simply:

$$\tau_o = 2\ \mu\ b/\lambda$$

where λ is the spacing of the precipitates on the glide plane which is of the order of $\sqrt{2r_pC_p}$ where r_p is the precipitate radius and C_p the volume concentration.

When a dislocation bypasses a precipitate and a ring of dislocations is left, the dislocation ring repels the next dislocation and the material hardens. Part of the recovery process is the removal of these rings.

Particles with lower elastic modulus than the matrix have lower Orowan stress in the particles, attract the dislocations. If the strength of the particle $\tau_p < 6\ \mu b/r_p$, then the dislocation will cut the particle rather than bypass it by the Orowan mechanism.

LECTURE 3

EVOLUTION OF CAVITY AND PRECIPITATE POPULATIONS

3.1 INTRODUCTION

The recovery and recrystallisation behaviour of real engineering alloys is intimately connected to the behaviour of precipitates. Precipitates, as we have seen, pin dislocations, impeding recovery and reducing the work hardening index. They also stabilise dislocation populations and subgrain boundaries, delaying the onset of primary recrystallisation. They also affect grain growth and in many alloys determine grain boundary mobilities. In this lecture we will prepare for Lecture 5 by laying down the basic principles of precipitate behaviour.

First of all, it is worth making some general remarks. In most alloys, there is some degree of solubility of elements that generate precipitate phases. There may be a solution temperature where the amount of alloying elements will completely dissolve, although this temperature may be above the melting point. Annealing above the solution temperature will produce a single phase material. Subsequent cooling will permit precipitation, although there will be a finite time to bring this about. For temperatures close to the solution temperature, the driving force for precipitation will be small, but the kinetics will be rapid. In these conditions, large precipitates will grow rapidly and continue to coarsen (ripen). For temperatures much lower than the solution temperature, the driving force for precipitation will be large, but the kinetics will be slow. Fine precipitates generally result in this case. In some systems diffusionless phase changes can occur, and these will occur spontaneously when the free energy difference is large enough. These are often called martensitic transformations. The best known and most important of these is in the iron-carbon system and the resulting distorted martensitic crystal structure is produced by the presence of interstitial carbon, which could produce carbides if there was time for diffusion. Figure 3.1a shows schematically a time-temperature-transformation diagram illustrating these points. In complex alloys, such as commercial stainless steels with many alloying elements, there will be overlapping sets of precipitating processes that interact with each other, see Figure 3.1b for an example.

3.2 PRECIPITATE NUCLEATION

Precipitation has three phases in its development:

(i) nucleation;
(ii) growth;
(iii) ripening (coarsening).

Coarsening can take place by coalescence permitted by some degree of mobility of precipitates, but we will discuss that later and restrict ourselves here to what is known as Ostwald ripening, i.e. coarsening by atomic diffusion. All three phases can, and do, occur simultaneously but from the point of view of modelling they are often treated separately and are assumed to occur separately.

Let us first look at the classical theory of nucleation of precipitates as developed for solid reactions by Turnbull. Nucleation can occur by random interactions of solute in the matrix and is then termed homogeneous nucleation; alternatively, nucleation can occur at preferred sites, which could be dislocations, grain boundaries or other interphase boundaries. In the latter case, the nucleation is said to be heterogeneous. In some cases heterogeneous nucleation can result in viable nucleii, but in most cases heterogeneous nucleation is considered in classical nucleation theory as having to overcome an energy barrier. This arises from a sensitivity of the free energy of an atom's cluster to the number of in the cluster. The energy barrier is manifested by a critical cluster size for nucleation. Clusters below the critical size are termed embryos, at the critical size are termed nucleii and at above the critical size precipitates.

The nucleation barrier arises because of interfacial effects; simply expressed, a small precipitate has a larger interfacial energy per atom than a large precipitate. This is a universal concept that applies to the nucleation of solids in melts, aerosols, cavities, bubbles, point defect clusters during irradiation, as well as precipitates in alloys. Transparency 3.1 outlines the details of the classical nucleation theory.

If we ignore the possibility of elastic strain energy for the moment, the free energy charge per unit volume is determined by the supersaturation of the solute. At the solution temperature,

$$\Delta G_v = \Delta H_v - T \Delta S_v = \Delta H_v \Delta T / T_s \qquad (3.1)$$

and $\Delta T = (T_s - T)$ is the degree of undercooling. In this case ΔG^* is inversely proportional to ΔT^2 so the height of the nucleation barrier decreases sharply below the solution temperature. For sufficiently low temperatures, nucleation is entirely determined by diffusional processes. The rate of nucleation therefore has a peak at some temperature below the solution temperature.

The chemical nucleation theory has been very successful in describing many features of nucleation of precipitates. However, it is not very compatible with calculations of the growth or ripening. A technique well suited to large scale computation has been introduced, known as hierarchical modelling. This technique has been very successful at investigating the early stages of nucleation, but is unsuitable for large clusters of atoms. A hierarchical scheme is illustrated in Transparency 3.2. Some progress has been reached recently in reconciling the two approaches and an outline is given in Transparency 3.3.

Some precipitations do not have nucleation in the classical sense, as there may be no barrier. Nucleation and growth then merge into a single problem. An example of this is precipitation onto flat platelets; here, both the volume of the precipitate and the interfacial energy are proportional to the area of the platelet, provided it grows at constant thickness. The shape of the precipitate will depend partly on the anisotropy of the interfacial energy and partly on the strain energy of the precipitate as it grows.

Coherent precipitates will always have some degree of misfit with the host lattice. Incoherent precipitates have a variable degree of hydrostatic strain interaction which will depend on whether any misfit can be relaxed by plastic or diffusive processes. The situation is quite complicated for small atomic clusters, where atom-atom interactions can render the simplistic description of a sphere in a continuum invalid. The free energy of the cluster will fluctuate wildly with the number of atoms and their configuration. There will always be some low energy clusters that will tend to persist. Despite this, the continuum description is surprisingly accurate at predicting the form and development of precipitation.

If the elastic moduli of the precipitate and the matrix are the same, there is no preference between spherical, flat or needle-like precipitates. When the precipitate is harder than the matrix, the spherical precipitate is favoured. When the precipitate is softer than the matrix, then a platelet is favoured. Needle-like precipitates are never favoured by strain energy, but often anisotropic interfacial energy or elastic effects can favour them.

Heterogensous nucleation occurs at a site when the free energy of small clusters can be reduced. This can be where the interfacial energy change is reduced at grain boundaries or other precipitates. If γ_{gb} is the interfacial energy of a grain boundary, the effective interfacial energy of a platelike precipitate is simply $\gamma_i - \gamma_{gb}$.

If the new precipitate wets an existing precipitate, i.e. when $\gamma_i + \gamma_{ab} < \gamma_b$, where γ_i is the interfacial energy between the new precipitate and the matrix, γ_{ab} the interfacial energy between the new and old precipitate and γ_b is the interfacial energy between the old precipitate and the matrix, then the effective interfacial energy for nucleation will be $\gamma_i - \gamma_b + \gamma_{ab}$. Also, the effective radius for nucleation will be the radius of the old precipitate, further enhancing the process. In this way, the nucleation barrier can be completely avoided. Other heterogeneous nucleation sites stabilise atomic clusters by offsetting strain energy contributions or by providing locally disturbed crystal symmetry. Dislocation cores or the regions immediately above or below edge dislocations may be favourable, and nucleation rates are enhanced by increased local concentrations of solute due to elastic interactions.

3.3 PRECIPITATE GROWTH AND RIPENING

The nucleation process will continue alongside growth until all the solute supersaturation is used up, but as precipitates grow they compete for solute, and if growth is limited by diffusion then growth will dominate over diffusion when $r_p C_p >> 2a c_a$.

For most purposes the expression:

$$\beta_n = 4\pi r_p D_a c_a \qquad (3.2)$$

is adequate to describe precipitate growth rates, but more accurately the recursive relation may be used:

$$\beta_n = 4\pi\, r_p\, [1 + r_p\, \sqrt{\beta_n C_p}]\, D_a\, c_a \qquad (3.3)$$

In some cases the growth will be limited by transfer of atoms at the interface between the precipitate and the matrix, in which case:

$$\beta_n = 4\pi\, K_a\, r_p^2\, c_a \qquad (3.4)$$

where K_a is the interfacial transfer velocity.

When precipitates are in the form of facetted polyhedra, the growth rate may be constrained by the number of sites on facets where solute atoms can be accepted. We will discuss this further when we describe the mobility of small particles.

Growth of precipitates on grain boundaries can be described simply if growth is limired by grain boundary diffusion of the solute:

$$\beta_n = \frac{4\pi\, \delta_{ga}\, D_{ga}\, c_a}{[4\, \ell n(C/r_p) - \tfrac{1}{2}(1-r_p^2/C^2)]} \qquad (3.5)$$

where δ_{ga} and D_{ga} are the effective width of the boundary and the boundary diffusion coefficient for the solute, C is the radius of the circle representing the area occupied by each precipitate on the boundary, and the radius of the precipitate on the boundary. When there are very few precipitates on the boundary and $C \gg r_p$, then we can use:

$$\beta_n = 2\pi\, \delta_{ga}\, D_{ga}\, c_a \qquad (3.6)$$

Growth of precipitates on boundaries can be limited by diffusion of solute to the boundary through the lattice, in which case:

$$\beta_n = 4\pi\, C^2\, D_a\, c_a / 3 d_g \qquad (3.7)$$

provided there is no trapping of the solute by other precipitates. Similarly, the expression for β_n can be found for precipitates lying on dislocations, where growth is limited by either dislocation pipe diffusion or to dislocations by lattice diffusion.

Ideally, to study growth of precipitates, we should set up a system of hierarchical equations and solve them for the whole range of precipitate sizes. However, this can only be done for studies of small atomic clusters, and some means of simplifying the problem must be found. Closed form solutions are possible, but only when $\beta_n < \alpha_n$ for large n, which is a case not directly of interest to us. The problem may be reduced by replacing individual classes of cluster by groups covering a range of sizes, and this is useful for some problems. Where there is no nucleation barrier, a moment analysis can be used, an example is shown in Transparency 3.4. Where there is a barrier to nucleation, a Fokker-Plank method can be used.

Treatments as described above will effectively cover nucleation, growth, ripening and dissolution if the supersaturation of the solute turns into a sub-saturation. For most modelling purposes however, much simpler descriptions of ripening and growth will suffice; the main problem being the fixing of the initial precipitate concentration. In these simplified treatments, a representative precipitate radius is used. Some examples of simplified growth and ripening expressions are given in Transparency 3.6

Precipitate ripening or coarsening is very important to the understanding of recovery and primary recrystallisation processes. Ripening kinetics for isolated precipitates are of the form $r_p \propto (D_a\, T)^{1/3}$, for grain boundary precipitates $r_p \propto (D_{ga} t)^{1/4}$, and for precipitates on dislocations $r_p \propto (D_{pa} t)^{1/5}$ or $(D_{pa} t)^{1/6}$ depending on the network configuration. This leads to great uncertainty on the time for critical coarsening and reduction in the apparent activation energy of the ripening process.

3.4 MOBILITY OF PRECIPITATES AND CAVITIES

The mobility of precipitates is perhaps a concept that does not come easily, but it is none the less important, as we shall see in determining grain boundary growth rates and in some circumstances precipitate coarsening. The mobility of cavities and bubbles is a special case with its own features.

Mobility of precipitates implies a transfer of material from one side of the precipitate to the other, see Figure 3.2. The precipitate mobilities for the various paths are described in Transparency 3.7. At any one temperature and precipitate size, a mobility mechanism will dominate. Figure 3.3 shows an example of a mechanism map for precipitate mobility.

Mobility of bubbles or cavities is different in that only the transport of matrix atoms is involved, see Figure 3.4. The presence of gas in the bubble has a profound effect on the bubble mobility. An example of bubble diffusion in stainless steel is shown in Figure 3.5. Additionally, small bubbles and precipitates are often facetted and not spherical. In this case the bubble or precipitate diffusivity is controlled by the nucleation of ledges on the surface of bubbles. The diffusivity is multiplied by:

$$L \exp(-\pi E L/2kT)$$

where L is the ledge length, $\sim r_b$, and E is the energy to nucleate a ledge. The correction for bubble or precipitate facetting is controversial and not yet fully understood.

3.5 GRAIN BOUNDARY MOBILITY

Grain boundary mobility is controlled by the intrinsic grain boundary mobility in the absence of precipitates, or by the driving force for boundary motion to break the boundary away from the precipitate. Otherwise, the grain boundary motion is dependent on the mobility of the precipitates.

The velocity of a precipitate is given by the Einstein equation:

$$v_p = D_p F_p/kT$$

where F_p is the force acting on the precipitate. The velocity of a grain boundary is given by:

$$v_{gb} = M_{gb} p_{gb}$$

where M_{gb} is the grain boundary mobility and p_{gb} is the pressure driving the

grain boundary motion, usually a grain boundary interfacial energy pressure. The force on a particle lying on the boundary is:

$$F_p = A_p p_{gb}$$

where A_p is mean grain boundary area per particle. If it is assumed that the boundary touches a random distribution of particles within a distance of r_p then:

$$A_p = 3 \pi r_p^2/3f$$

where F is the volume fraction of precipitate. For purely grain boundary precipitates A_p would be defined in terms of a grain boundary precipitate density.

When grain boundaries are pinned by particles, the grain boundary mobility is simply:

$$M_{gb} = D_b A_p/kT$$

If the force on the particles is large enough the grain boundaries can break away. Zener proposed a mechanism for unpinning where the force on the particle exceeded the force needed to break the interfacial energy:

$$F_p > \pi r_p \gamma_i$$

This leads to the relationship:

$$p_{gb} > 3 f \gamma_i/2 r_p$$

Rios has evaluated another model based on the boundary sweeping through a population of precipitates and bypassing them by bending around the particle and enclosing it in the same way as the Orowan mechanism for dislocations. The criterion for breakaway in this case (in normal grain growth) is:

$$r_p > 6 f R_{gb}$$

where R_{gb} is the grain boundary radius. In practice, this is about an order of magnitude larger than the Zener model and closer to experimental observations. A mechanism map for regimes of grain boundary mobility is shown in Fiture 3.6, and micrographs of grain boundary bubble and precipitate interactions are shown in Figures 3.7a and b. Ripening control is where particle mobility is low, but ripening eventually results in the boundary being liberated when the precipitates grow beyond the critical zone.

The mobility of grain boundaries is also influenced by solutes in a similar way to that of dislocations. Solutes segregated to grain boundaries will limit the intrinsic mobility as the solutes are dragged along with the boundary. At sufficiently high pressures on the boundary the boundary may break away, ~~see Figure 3.7~~. The intrinsic mobility of boundaries is determined by the diffusion of atoms across the boundary thickness (a relatively low energy process) and the intrinsic mobilities can be very high.

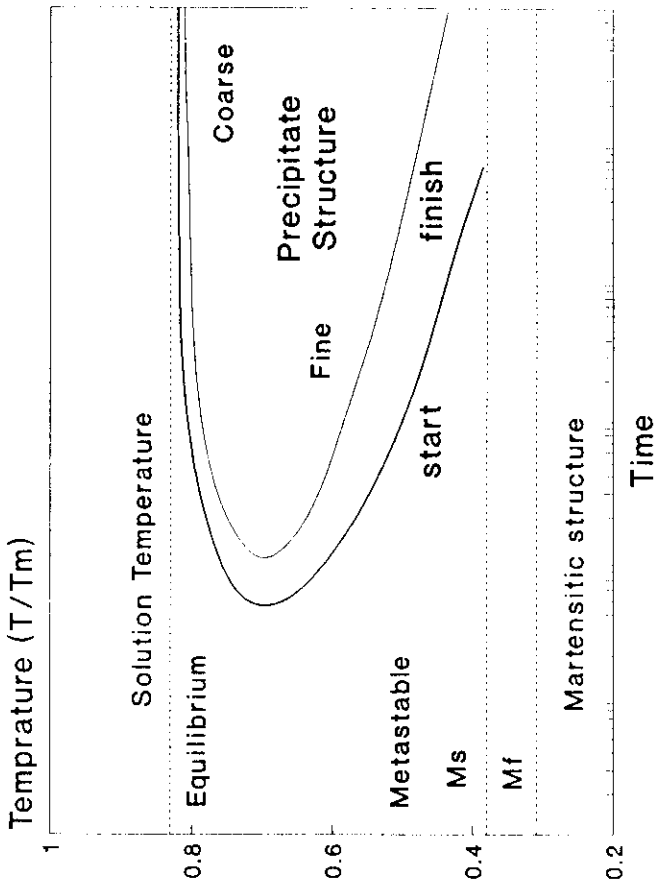

Fig. 3.14 Schematic time-temperature-transformation diagram.

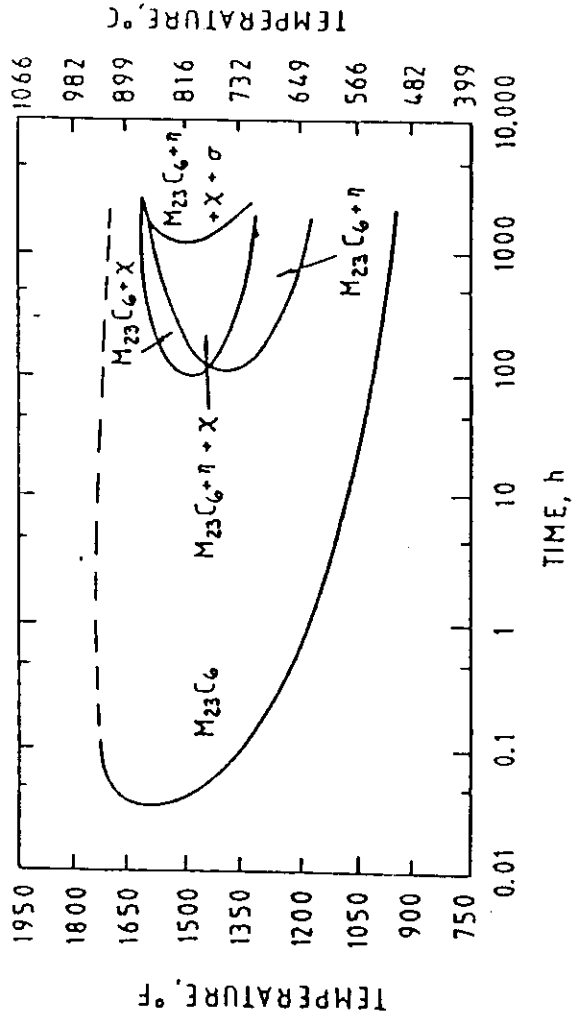

Fig 3·4 Time-Temperature-Precipitation diagram for Type 316 steel.

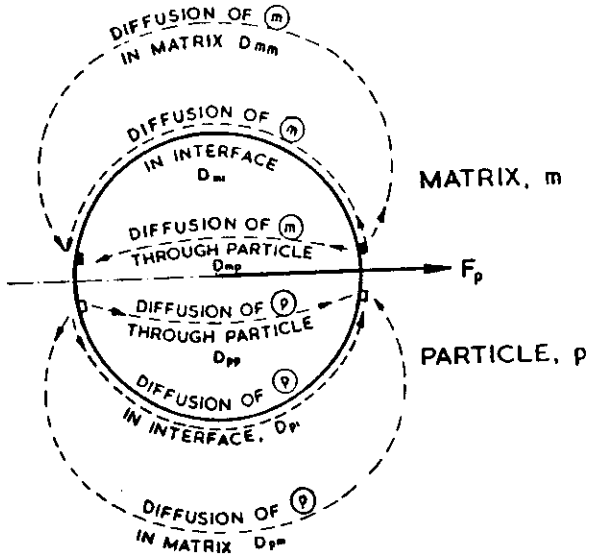

Fig. 3·2 Diffusion paths

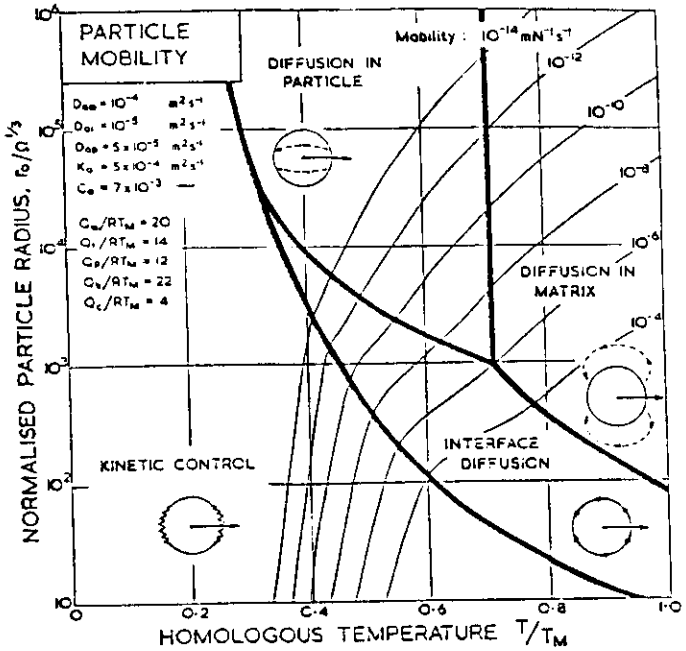

Fig. 3·3 Particle mobility map (Ashby)

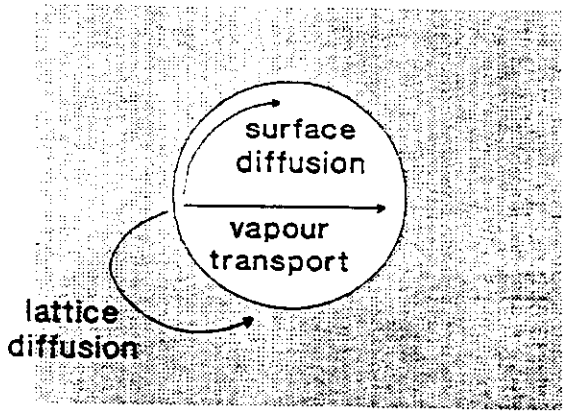

Fig. 3.6 Diffusion paths for cavities and bubbles.

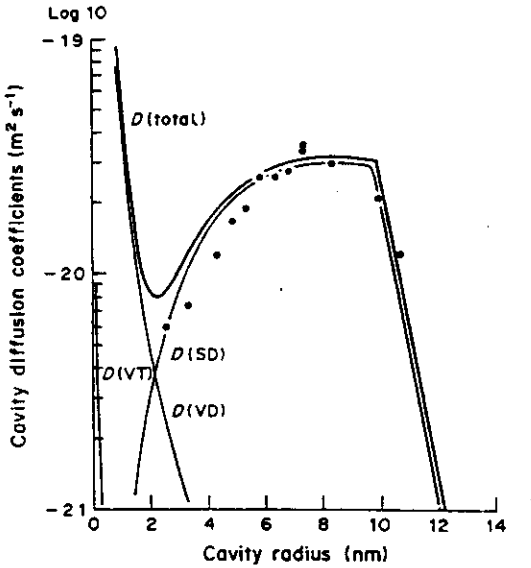

Fig. 3.5 Cavity migration in an austenitic steel. Experimental data (●) from Walker [10] and lines given by equations in text. (Goodhew)

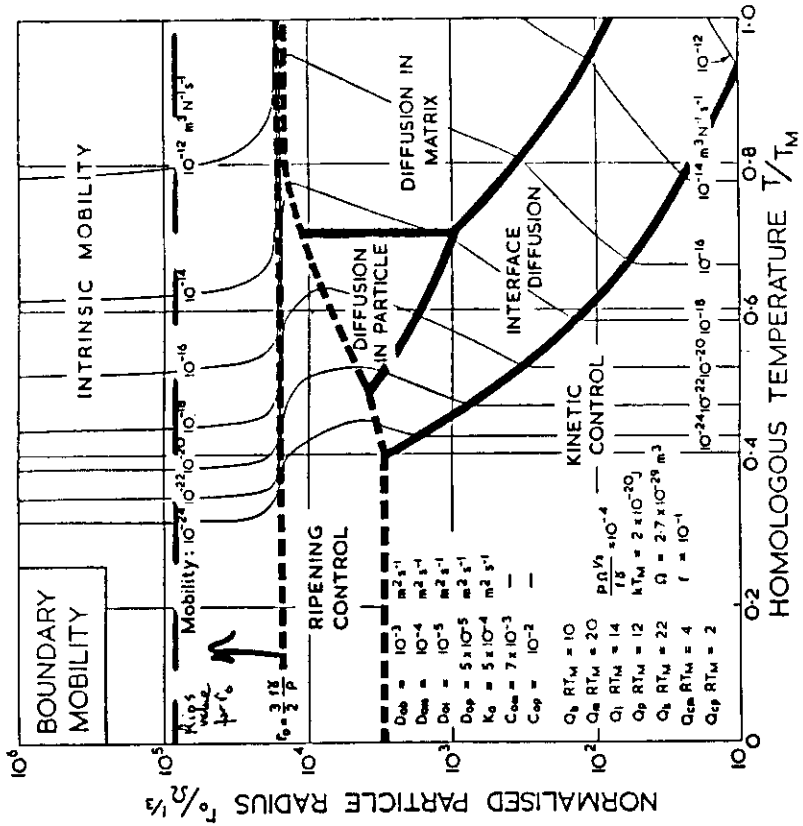

Fig. 3.6 Grain boundary mobility maps.

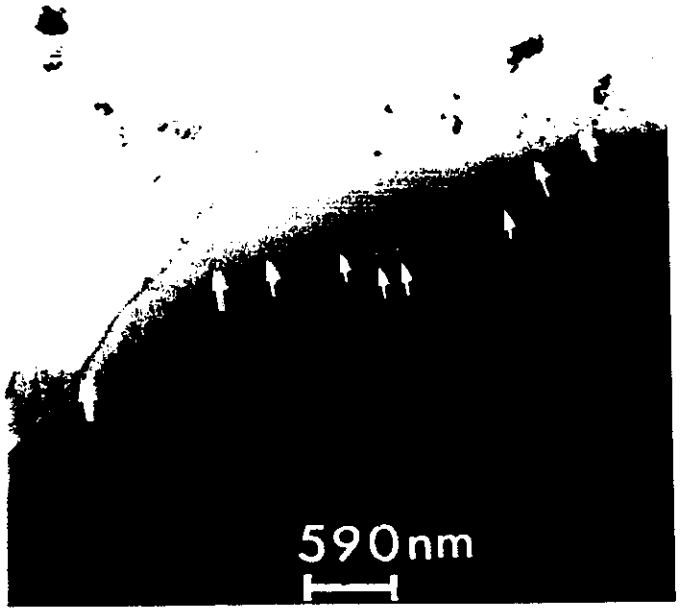

Fig. 3.7a Grain boundary breaking away from helium bubbles in stainless steel irradiated. (A.C. Roberts, Harwell)

Fig. 3.7b Grain boundary precipitate being dragged by boundary. Nb stabilised stainless steel at 1050°C. Electron micrograph (x3446) (A.J. Bunn, Harwell)

TRANSPARENCY 3.1

Classical Nucleation Theory

The simplest case is for spherical precipitates where the precipitate free energy is given by:

$$\Delta G_p = 4\pi r_p^2 \gamma_i + 4\pi r_p^3 \Delta G_v/3$$

ΔG_v is the free energy change per unit volume. This is made up of the chemical free energy change per molecule divided by the molecular volume and the local increase in elastic strain energy. ΔG_v must be negative overall for nucleation to occur. ΔG_p goes through a maximum as the size of the precipitate increases, ~~see Figure 3.1~~. The height of the maximum ΔG^* is a measure of the nucleation barrier:

$$\Delta G^* = 16 \pi \gamma_i^3/3 \Delta G_v$$

and the embryos have to reach the critical size r_n to become nuclei:

$$r^* = -2 \gamma_i/\Delta G_v$$

The nucleation rate is given by the rate at which embryos take the final step over the barrier to become nuclei:

$$\dot{N} = N_o A^* \tau \exp(-\Delta G^*/kT) \exp(-H_{am}/kT)$$

where τ is the atomic vibrational frequency ($\sim 10^{13} s^{-1}$), A^* is the number of sites at which an atom can join the embryo, N_o is the density of possible sites for nucleation, and H_{am} is the activation enthalpy for migration of a solute atom.

TRANSPARENCY 3.2

Hierarchical Nucleation and Growth Models

We follow the notation of Fell and Murphy.

The hierarchical equations lok at the growth of clusters of atoms of each size and the transfer of atoms from one size to the next:

$$\dot{C}_1 = G - 2\beta_1 C_1 - \sum_{n=2}^{\infty} b_n C_n + \sum_{n=2}^{\infty} \alpha_n C_n$$

$$\dot{C}_2 = \beta_1 C_1 - \alpha_2 C_2 - \beta_2 C_2 + \alpha_3 C_3$$

$$\dot{C}_3 = \beta_2 C_2 - \alpha_3 C_3 - \beta_3 C_3 + \alpha_4 C_4$$

$$C_n = \beta_{n-1} C_{n-1} - \alpha_n C_n - \beta_n C_n + \alpha_{n+1} C_{n+1}$$

where G is any source term, β_n is the probability for unit time that a cluster size n accepts an atom and moves to size n+1, α_n is the probability that n rejects an atom and moves to size n-1.

$$\beta_n = 4\pi D_a c_a r_n$$

and

$$\alpha_n = \beta_n (c_e/c_a)[(n-1)/n] \exp[-(\Delta G_n - \Delta G_{n-1})/kT]$$

where C_e is the equilibrium concentration of a and r_n is the radius of a cluster size n.

$$c_e/c_a = \exp(-\Delta H_v \Omega_a (T_s - T)/kTT_s)$$

$$\Delta G_n - \Delta G_{n-1} = 2 \gamma_i / r_n$$

TRANSPARENCY 3.3

Reconciliation of Classical and Hierarchical Theories

Clement and Wood have shown how the classical and hierarchical theories of nucleation can be reconciled for the case of steady state nucleation.

In this case:

$$\dot{N} = \beta_1 C_1 - \alpha_2 C_2 = \beta_2 C_2 - \alpha C_2 = \text{-----} = \beta_{m-1} C_m - \alpha C_m$$

up to the critical nucleation size, assuming C_1 is approximately constant. A real barrier is needed for the nucleation process:

$$J = \beta_1 C_1 \left(1 + \sum_{n=2}^{\infty} \prod_{j=2}^{n} \alpha_j/\beta_j\right)^{-1}$$

After some approximation:

$$\Delta G^* = \Delta G_p (n_c) = 16 \pi g_i^3 [T_s/\Delta H_v (T_s - T)]^2$$

$$n_c = (3^2\pi/3 \Omega_a) [\gamma_i T_s/\Delta H_v (T_s - T)]^3$$

which is derived from $dG_p(n)/dn=0$ when

$$\Delta G_p(n) = kT[1/3 \ln(n_c/n) - n \ln(c_a/c_e)] + \Delta G_n$$

The nucleation rate is:

$$\dot{N} = -\frac{1}{2\pi kT} \frac{d^2}{dn^2} \Delta G_p (n)^{1/2} \beta_{nc} (2 \Omega_a^2/4\pi)^{1/2} \exp(-\Delta G^*/kT)$$

TRANSPARENCY 3.4

Moment Analysis for Precipitate Growth with no Nucleation Barrier

All clusters of atoms of two or above are considered as precipitates, and the population is characterised by three quantities: the total number of precipitates $C_p = \sum_{n=2}^{\infty} C_n$,

the mean number of atoms per precipitate $\bar{n} = \sum_{n=2}^{\infty} n C_n/C_p$,

and the second moment of the distribution $M_2 = \sum_{n=2}^{\infty} (n-\bar{n})^2 C_n/N$. Expanding β_n and α_n about their values at n, and putting in a set of hierarchy equations, the following set of equations can be obtained after neglecting moments higher than the second:

$$\frac{dC_1}{dt} = G - \frac{d(\bar{n} C_p)}{dt}$$

$$\frac{dC_p}{dt} = \beta_1 C_1 - \alpha C_2$$

$$\frac{d(nC_p)}{dt} = C_p (\beta_n - \alpha_n) + \frac{M_2 C_p}{2} \frac{d^2}{dn^2} (\beta_n - \alpha_n)_{\bar{n}} + 2\beta_1 C_1 - \alpha_2 C_2$$

$$\frac{d}{dt} (M_2 C_p) = C_p(\beta_n - \alpha_n) + \frac{M_2 C_p}{2} \frac{d^2}{dn^2} (\beta_n + \alpha_n) + 2M_2 C_p \frac{d}{dn} (\beta_n - \alpha_n) \bar{n}$$

$$+ (\bar{n}-2)^2 \beta_1 C_1 - (\bar{n}-1)^2 \alpha_2 C_2$$

These equations can now be solved numerically fairly easily, except that a value is needed for C_2. This is dealt with by assuming a distribution of sizes of precipitates, e.g. log-normal:

$$C_2 = C_p \int_{1.5}^{2.5} P(n) dn$$

and

$$P(n) = \frac{1}{n\sigma\sqrt{2\pi}} \exp\ \frac{[-[\ln(n-1.5)-\bar{n}]^2}{2\sigma^2}$$

$$\bar{n} = 1.5 + \exp(\mu + \sigma^2/2)$$

$$M_2 = \exp(2\mu)\ \exp\ (\sigma^2)\ [\exp(\sigma^2)-1]$$

μ and σ^2 are the mean and standard deviation of the corresponding normal distribution and an offset of 1.5 has been used.

TRANSPARENCY 3.5

Fokker Plank Equations for Growth of Precipitates

The Fokker–Plank Equation is:

$$\frac{\partial}{\partial t} C(n,t) = -\frac{\partial}{\partial n} J(n,t)$$

where the flux of atoms through the distribution is:

$$J(n,t) = \mathcal{F}\, C(n,t) - \frac{\partial}{\partial n}[\mathcal{D}\, C(n,t)]$$

The first term $\mathcal{F} = \beta_n - \alpha_n$ is the drift term and the second term is $\mathcal{D} = \frac{1}{2}(\beta_n + \alpha_n)$ which is the drift term.

Hierarchy equations can then be used to generate the growth of small clusters up to a value n_c. Larger clusters are described by:

$$\frac{d}{dt} C_p = J(n_c,t)$$

$$\frac{d\bar{n}}{dt} = \frac{1}{C_p}[(n_c-\bar{n})J(n_c,t) + \mathcal{D}\, C(n_c,t)] + \mathcal{F}$$

$$\frac{dM_2}{dt} = [(n_c-\bar{n})^2-M^2]\frac{J(n_c,t)}{C_p} + 2\mathcal{D}\left[\frac{(n_c-\bar{n})C(n_c,t)}{C_p} + 1\right].$$

The drift and dispersion terms are evaluated at $\bar{n}$ and $C(n_c,t)$ is found by assuming a distribution function – as in the case of the moment method.

The nucleative flux is:

$$J(n_c,t) = \beta_{nc-1}C_{nc-1} - \alpha_{nc}C_{nc}.$$

The value of n_c is chosen by finding n where $\alpha_n = \beta_n$ or by choosing a sufficiently large value.

TRANSPARENCY 3.6

Simplified Growth and Ripening Equations

Initial phase of growth where solute is not depleted

$$\frac{dr_p}{dt} = D_a\Omega_a(C_a - C_e)/r_p,$$

$$r_p \sim (D_a t)^{\frac{1}{2}}.$$

As the solute is used up the concentration varies as:

$$\frac{d}{dt} C_a = -\frac{d}{dt} (\bar{n}C_p) = -(4\pi)^{2/3}(3\Omega\,\bar{n})^{1/3}\, C_p D_a(C_a - C_e).$$

For surface transfer controlled growth

$$\frac{dr_p}{dt} = K_a\Omega_a(C_a - C_e)$$

and for growth on grain boundaries

$$\frac{dr_p}{dt} = \frac{\delta_{ga} D_{ga}\Omega(C_a - C_e)}{2r_p^2}.$$

Ripening is the growth of the precipitates by the transfer of solute from the smallest members of the population to the largest driven by the interfacial energy.

For ripening by lattice diffusion we may use Greenwood's expression:

$$\frac{dr_p}{dt} = \frac{\alpha_r D_a C_e \Omega_a^2 \gamma_i}{r_p^3\, k\, T}$$

where α_r is a constant between 1/3 and 3.

For ripening of grain boundary precipitates

$$\frac{dr_p}{dt} = \frac{\alpha_r \delta_{ga} D_{ga} C_e \Omega_a^2 \gamma_i}{r_p^3\, k\, T}$$

where in this case α_r varies between 1/20and 2 and is dependent on the shape of the precipitate.

TRANSPARENCY 3.7

Precipitate Mobility

Diffusion in the matrix

solute diffusion

$$D_{ma} = 3\, C_a D_a \Omega/4\pi\, r_p^3$$

matrix lattice diffusion

$$D_{mm} = 3D_L\Omega/4\pi\, r_p^3.$$

Diffusion in the matrix precipitate interface

$$D_{im} \text{ or } D_{ia} = 3\, \delta_i D_i \Omega/2\pi r_p^4.$$

Diffusion in the precipitate

precipitate atom diffusion

$$D_{pa} = 3D_{Lp}\Omega/4\pi\, r_p^3$$

matrix atom diffusion

$$D_{pm} = 3\, C_m D_m \Omega/4\pi\, r_p^3.$$

Interface reaction control

$$D_{km} \text{ or } D_{ka} = 3K\Omega/2\pi r_p^2.$$

The various contributions to bubble diffusivity are combined by:

$$D_m = \left[\frac{1}{D_{mm}+D_{im}+D_{pm}} + \frac{1}{D_{ma}+D_{ia}+D_{pa}} + \frac{1}{D_{km}} + \frac{1}{D_{ka}}\right]^{-1}$$

TRANSPARENCY 3.8

Mobility of Cavities and Bubbles

Lattice diffusion

$$D_{b_L} = 3D_L\Omega/4\pi r_b^3$$

Vapour transport

$$D_{b_V} = 3\,\Omega^2\beta P_{vap} D/4\pi\, kT\, r_b^3,$$

where β is the departure from gas ideality, P_{vap} is the vapour pressure of the matrix and D_g is the diffusivity of vapour in the gas which is dependent on the gas pressure.

Surface diffusion

$$D_{bs} = 3\delta_s D_s \Omega\, W(n_b)/2\pi\, r_b^4$$

where $W(n_b)$ is a parameter controlled by the presence of gas atoms interfering with the surface diffusion.

$$W(n_b) = \exp\left[-\frac{3n_bQ}{4\pi r_b^3}\left[1 + \frac{2y}{(1-y)^2} + \frac{2y^2}{(1-y)^3}\right]\right]$$

where Q is an interaction parameter which is dependent on gas and vapour species.

$$D_b = D_{b_L} + D_{b_V} + D_{bs}$$

LECTURE 4

MODELLING DISLOCATION POPULATION EVOLUTION

4.1 INTRODUCTION

In this lecture we will look at the formation of low energy dislocation configurations using different modelling techniques. Each technique has its limitations and we have yet to develop a fully satisfactory set of tools for reproducing all aspects of dislocation behaviour.

The first technique we will look at is the modelling of the dynamics of individual dislocations and their interactions. This can only be done by making some major approximations. Despite this, many features of observed structures can be reproduced. The second technique avoids describing the spatial variations but uses reaction kinetics (or rate theory) to look at the average behaviour of the material. In this way the structural changes can be used to predict macroscopic properties. The third technique is the modelling of spatial variations of dislocation density by continuum methods. This technique is in its infancy and has the potential of being a very powerful tool.

4.2 DISLOCATION DYNAMICS MODELLING

We will use the work of Amodeo on two dimensional arrays of straight dislocations to illustrate this technique. In principle, the modelling of three dimensional dislocation interactions is possible, but will require enormous computing power to be useful. A simplified model of the two dimensional dislocation population behaviour has been prepared for these lectures as a BASIC program that permits an interactive animated display of the dislocations on a PC screen. This program permits the effects of ratio of climb to glide mobilities, flow stress and applied stress to be investigated.

For a two dimensional simulation the following items are required:

(a) Dislocation Configuration

First of all, the dislocation system has to be specified. In most of the examples given below either sets of dislocations with the same Burgers vectors, but with mixed signs or sets of orthogonal dislocations are used.

There is no reason why real slip systems cannot be simulated, but once dislocations on different glide planes interact and dislocations bow out, they cannot be treated as points representing straight lines. A meso-scale model of curved dislocations is required, but no bright suggestions have been made yet.

(b) The forces on the dislocations

These forces arise either from the mutual interaction of the dislocations or from an applied stress. The forces between dislocations are described in Transparencies 2.1 and 2.2. The forces are resolved into climb and glide components and summed up for each dislocation.

(c) A boundary condition

Two boundary conditions are commonly assumed. The dislocation can be contained in a repulsive box, where it feels a repulsive force as it approaches the box boundaries. This boundary condition can represent the ? image forces for a surface or a grain boundary. Alternatively, a periodic boundary can be applied.

(d) Dislocation mobility

The velocity of each dislocation is calculated from the forces and the dislocation mobilities. In Amadeo's DISLODYN model, realistic mobilities are calculated representing the true mobilities of dislocations in real materials for a given temperature. In the simplified model used in the demonstrations, only the ratio of climb to glide mobilities is specified, but a threshold stress is applied to glide to account for the material flow stress.

(e) Definition of dislocation interactions

Before modelling starts, the range of dislocation interactions has to be specified. Dislocations of opposite sign that come within a critical distance:

$$y_s = \mu\, b/2\pi\, \tau_c$$

will annihilate. If they are a slightly larger distance they may be immobilised and form a dipole, or if the local stress on the dislocations is large enough they may pass by one another. Dislocations of the same sign will attract one another if they come within the zone defined in Figure 2.3c. Edge dislocations of different Burgers vector are generally attractive and will form a lock if they come within a similar distance y_s. Locked dislocations can be unlocked by the arrival of a dislocation of opposite sign to one of the locked dislocations.

(f) Other features

Dislocation sources can be introduced where a new dislocation is generated if the local stress is above some critical value representing say, a Frank-Read source.

(g) Time steps

The evolution of the dislocation population is described by taking short time steps over which each dislocation moves a distance determined by its velocity. At the end of the time step the forces and velocity are recalculated for the new positions. In the simple model, a fixed timestep is used, but in a DISLODYN a complicated set of criteria are used to ensure that no distribution reaction is missed due to too large a dislocation movement.

Such dislocation dynamics models can be used to study a wide range of dislocation patterning behaviour, where there is no dominant three-dimensional interaction. Figure 4.1 shows a sequence from the DISLODYN model for the generation of persistent slip bands in fatigue in copper at 25°C. Figure 4.2. shows a sequence describing dislocation cell formation in iron at 600°C. The data used in the calculations are given in the attached Tables.

4.3 SUBGRAIN FORMATION AND DESTRUCTION

The formation of subgrains results in a reduction in elastic energy compared with a random or uniform distribution of dislocations. If we take the example of a heavily cold worked material, the dislocations will form sub-grains of a

characteristic size during recovery. However, this is not an equilibrium condition and continued annealing will result in a continued coarsening of the subgrain structure. The driving force for this can be seen by looking at the energy per dislocation in the boundary:

$$E \text{ (per dislocation)} = \frac{\mu b^2}{4\pi(1-\nu)} \ln \frac{h}{b}$$

or

$$= \frac{\mu b^2}{4\pi(1-\nu)} \ln \frac{1}{b\rho_b d}$$

where h is the spacing of dislocations in the boundary, ρ_b is the density of sub-boundary dislocations and d is the sub-boundary diameter.

Holt has shown that a uniform distribution of dislocations is unstable to any small perturbation, and this will result in a heterogeneous structure with a characteristic wavelength. He looked at perturbations in the dislocation density for the continuity equation.

We will return to his method under continuum models in Section 4.5, but for the moment we will note that the wavelength for the dislocation clustering has value which is proportional to $1/\rho_o^{\frac{1}{2}}$, ρ_o being the initial dislocation density. This technique, however, cannot provide the constant K_c in the empirical observation:

$$d = K_c/\rho_o^{\frac{1}{2}}$$

Values of K_c measured for iron are typically around 5 and this compares well with values of around 6.4 to 8.4 estimated from the DISLODYN model.

Gittus has used a free energy minimisation argument to arrive at a value for K_c This requires a specific model for creep and has the unexpected result:

$$K_c \sim 1.58/C_j^{0.4}$$

This gives the observed values of K_c for rather unrealistically high values of C_j.

The key to the understanding of subgrain size during creep is that there is a continuous process of subgrain nucleation and destruction. Subgrains are mobile and their mobility will be a function of their complexity. The mobility will be constrained by the slowest moving components and will inevitably involve climb processes as well as glide. In real materials the subgrains may act as precipitate nuclei and will also tend to have saturated solute atmospheres. Subgrains will coarsen in a similar way to grain boundaries. The driving pressure will be the boundary energy and the smallest grains will disappear first.

The description of subgrain growth and destruction in the lecture is taken from Section 2.6 of the paper entitled "A Dislocation Model for Creep in Engineering Materials" by Ghoneim, Matthews and Amodeo, which is appended to these notes.

4.4 REACTION KINETICS MODELLING OF CREEP AND RECOVERY

The description of reaction kinetics modelling of creep with subgrain formation is taken from the Ghoneim, Matthews and Amadeo paper. Transparency 4.1 gives an overview of the rate equation used to form the CREEP computer program. Figure 4.3 shows an example of the stress distribution found within subgrains, taken from the work of Gibeling and Nix.

4.5 CONTINUUM MODELLING OF DISLOCATION SPATIAL DISTRIBUTIONS

Continuum modelling of dislocation distributions is as yet only in its infancy. There is a need for a good tensor to represent the dislocation distribution. The Nye tensor is inadequate as it only permits the net excess crystal distortion to be monitored, which is fine for lattice curvature calculations, but is not of much use for plasticity studies. The dislocation loop tensor is more useful, but has some drawbacks. Much of the work done so far has used the Scalar dislocation density. Despite this, many of the results have been impressive. The main technique has been to perturb a uniform dislocation distribution to look for symmetry breaking effects with dominant growth behaviour.

We will start with the continuity equation:

$$\frac{d\rho}{dt} + \text{div} \quad \mathbf{J} \quad = G$$

where J is the dislocation flux and G is some generalised source or loss term for the dislocations. J will have contributions from drift of dislocations in any elastic field and a diffusive term:

$$J = -\frac{\rho D_d}{kT} \text{ grad } E + D_d \text{grad}\rho$$

where D_d is the dislocation diffusivity = kTM_g or kTM_c.

Holt in his analysis of dislocation cell formation, just used the drift term. He considered that on average dislocations of positive and negative sign were equal, but locally there would be a distribution f(r) dependent on the overall dislocation density that favoured dislocations of opposite sign close to a particular dislocation, and slightly disfavoured them further away, bit that beyond a radius r_c there would be equal numbers, see Figure 4.4. The elastic interaction energies of dislocations would be described by:

$$E_I = \int_{r_o}^{r_c} r_i f(r)\, \mu b^2\, \ell n\, (R_o/r) dr$$

where r_o is the dislocation core radius and R_o the overall crystal radius. A dislocation distribution in space is now considered as a perturbation of a uniform distribution ρ_o, i.e. $\rho(x,y) = \Delta\rho(x,y)$. Up to several order terms the interaction energy fluctuation is:

$$\Delta E_I = F_1 \Delta\rho - F_2 \nabla^2 \Delta\rho$$

where

$$F_1 = \int_{r_o}^{r_c} (r/\rho_o) f(r)\, \mu b^2\, \ell n(r_o/r) dr$$

$$F_2 = \int_{r_o}^{r_c} (r^3/4\rho_o)\, f\,(r)\, \mu b^2\, \ell n(R_o/r) dr$$

If there are no source terms then from the continuity equation neglecting the diffusive term:

$$\frac{\partial \Delta\rho}{\partial t} = \rho D_d [F_1 \nabla^2 \Delta\rho + F_2 \nabla^4 \Delta\rho]$$

The solutions of this equation are:

$$\Delta\rho = A(\beta) \exp(Bt) \cos(\beta.r)$$

$$B = \rho D F_1 \beta^2 - \rho D F_2 \beta^4$$

the fastest growing value of β is given by $\beta^2 = F_1/2F_2$ with a characteristic wavelength $\lambda_m = 2\pi(2F_2/F_1)^{\frac{1}{2}}$. Any reasonable choice of f(r) gives $\lambda_m \propto r_c \propto \rho_o^{-\frac{1}{2}}$. Aifantis and co-workers have used the diffusive part of the continuity equation. They also split the dislocations into mobile and immobile populations with a particular model for the exchange of dislocations between the two populations:

$$\frac{d\rho_i}{dt} = g(\rho_i) - b\,\rho_i + \gamma\rho_m\rho_i^2 + D_i \nabla^2\rho_i$$

$$\frac{d\rho_m}{dt} = b\,\rho_i - \gamma\rho_m\rho_i^2 + D_m \nabla^2\rho_m$$

As can be seen from these equations, the immobile population is the only real source of new dislocations. There is no annihilation term. Mobile dislocations are immobilised at a rate determined by the interaction term $\rho_i\rho_m$ and the local stress, which is determined by the immobile dislocation density. The remobilisation of immobile dislocations is found to be a critical parameter. These particular choices of terms are only one of a range that could have been chosen, but they have proved useful in the understanding of persistent slip bands (see Walgraef and Aifantis in Res Mechanica 23 (1988)161) for a description. However, even the analysis of homogeneous steady state perturbations in one dimension have given the encouraging result that there is a characteristic wavelength which can be shown to be proportional to $1/\rho_i^{\frac{1}{2}}$.

The above model can be further elaborated by differentiation between dislocations of opposite sign. So far, continuum models have been handicapped by a lack of ability to deal with local interactions whose rate is determined by small scale heterogeneities.

Transparency 4.1

CREEP Model with Sub-grain Boundary Kinetics

Creep Strain-Orowan Equation

$$d\epsilon/dt = b\rho_m v_g$$

Mobile Dislocation Density

$\partial\rho_m/\partial t$ = Production from the mobile population and subgrain walls — annihilation at subgrain walls — climb recovery — dynamic recovery

$$\frac{\partial\rho_m}{\partial t} = v_g\left[\rho_m^{3/2} + \frac{\beta R_{sb}}{h^2} - \frac{\rho_m}{2R_{sb}} - B\rho_m^{3/2}\left(\frac{v_{cm}}{v_g}\right) - \delta\rho_m(\rho_m + \rho_s)\right]$$

Static Dislocation Density

$\partial\rho_s/\partial t$ = Immobilization rate at subgrain walls — climb recovery — dynamic recovery

$$\frac{\partial\rho_s}{\partial t} = v_g\left[\left(\frac{\rho_m}{2R_{sb}}\right) - B\frac{\rho_s}{h}\left(\frac{v_{cs}}{v_g}\right) - \delta\rho_m\rho_s\right]$$

Boundary Dislocation Density

$\partial\rho_b/\partial t$ = Production from static population — annihilation by creation of new subgrain surface

$$\frac{d\rho_b}{dt} = B(1 - 2\zeta)\rho_s\frac{v_c}{h} - \left(\frac{\rho_b}{R_{sb}}\right)M_{sb}(p_s - 2\pi r_p^2 N_p\gamma_{sb})$$

Subgrain Radius

dR_{sb}/dt = Growth by reduction of surface energy — shrinkage by nucleation

$$\frac{dR_{sb}}{dt} = M_{sb}(p_s - 2\pi r_p^2 N_p\gamma_{sb}) - \mu\eta_v K_c R_{sb}\left[(\rho_m + \rho_s)^{1/2} \cdot \frac{K_c}{2R_{sb}}\right]\frac{\Omega D_s}{kT}$$

TABLE 1
Data for PSB Simulation Cases

Material	Copper
Dipole width	$130b$
Annihilation width	$65b$
vssr	112/15
Applied stress	30 MPa
Initial dislocation density	$2{\cdot}86 \times 10^{10}\,cm^{-2}$
Friction stress	5 MPa
Temperature	25 °C

TABLE 2
Data for Dislocation Cell Simulation Cases

Material	Iron
Dipole width	$130b$
Annihilation width	$65b$
Junction width	$40b$
Applied stress	100 MPa
Initial dislocation density	$4{\cdot}00 \times 10^{10}\,cm^{-2}$
Friction stress	14 MPa
Temperature	600 °C
Initial dislocations	400
Dimensions	$1\,\mu m^2$

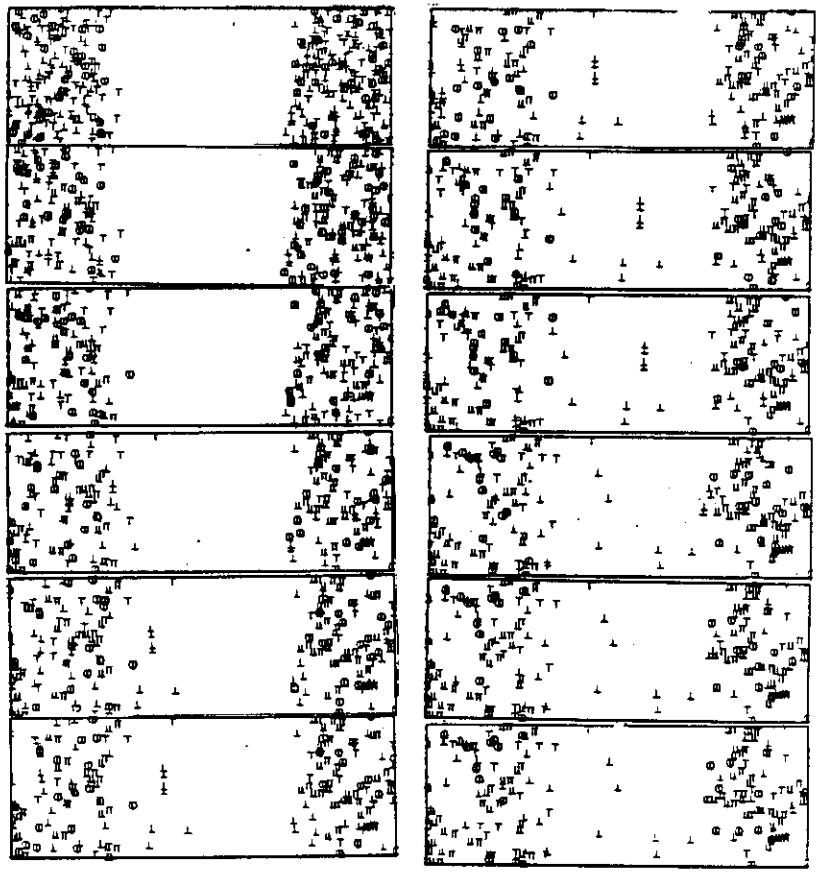

Figure 4-1: Dynamic Simulation of PSB Formation Including Random Multiplication

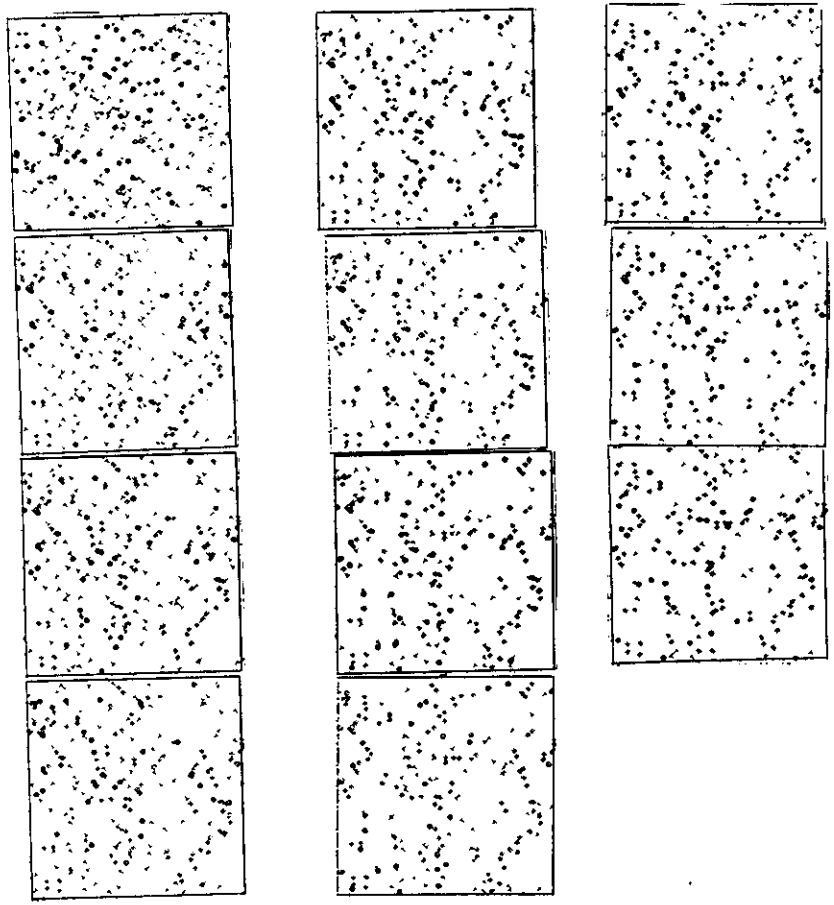

Figure 4-2: Simulation of Cell Formation (sequence 1): 600° C, 100 MPa, $4 \times 10^{10}/cm^2$

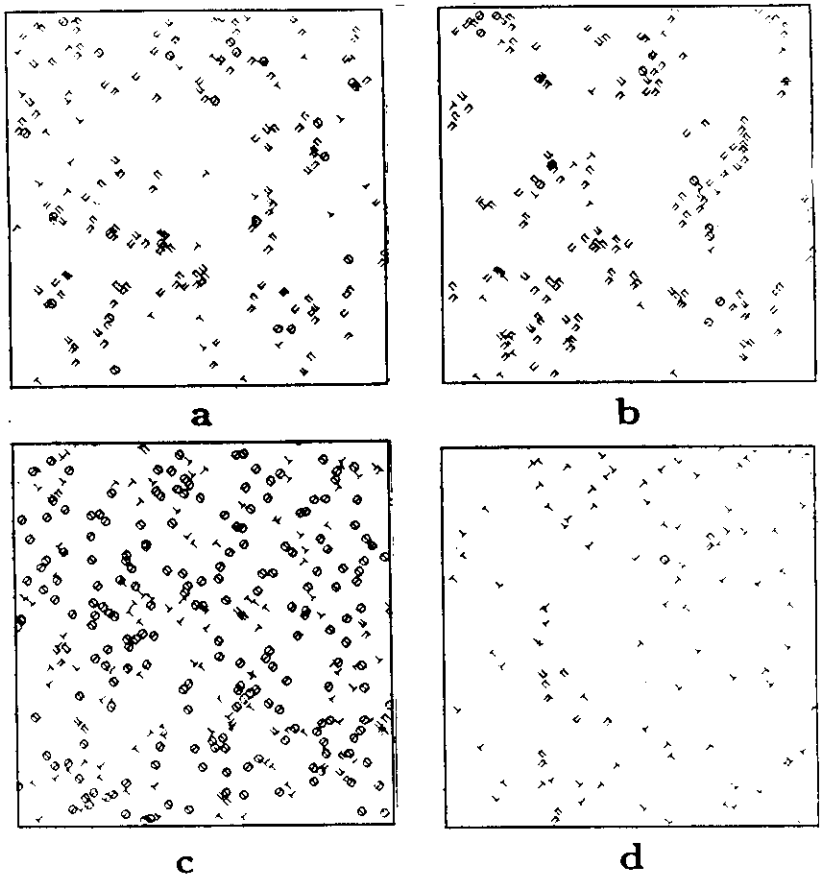

Figure 4·2a Dislocation Cells : a,b: high temperature, high stress; c: low temperature, low stress, d: low dislocation density

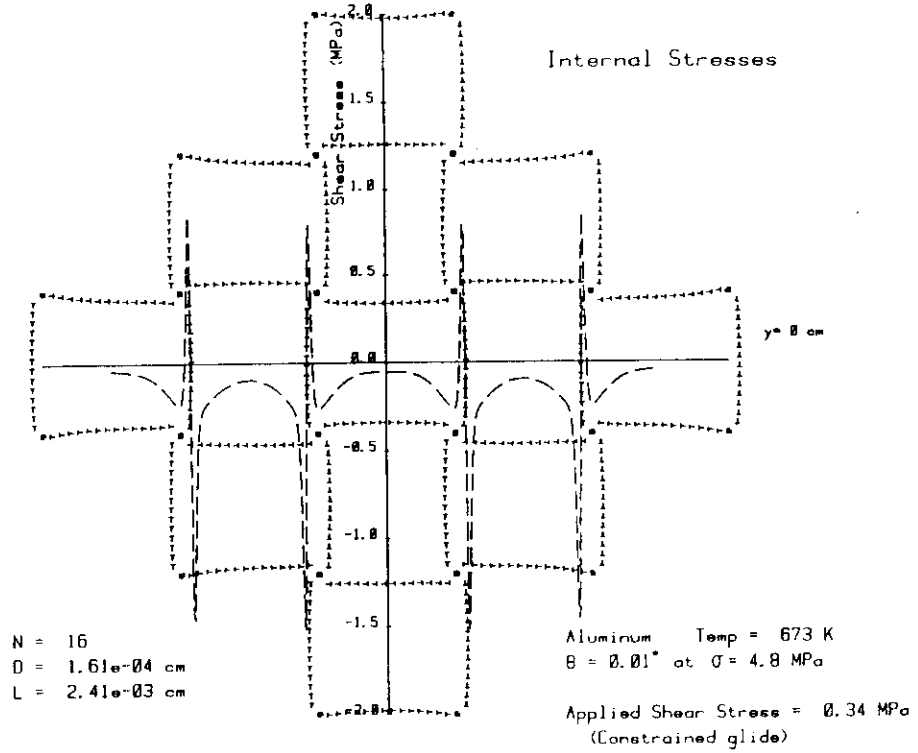

Fig 4·3 Configuration of sub-boundaries for an array of subgrains under an applied shear stress of 0.34 MPa (50 psi). The internal shear stress as a function of x at y = 0 is also illustrated (dashed line).

LECTURE 5

MODELLING RECRYSTALLISATION

5.1 INTRODUCTION

Modelling of recrystallisation is not as well developed as the modelling of dislocation substructures. This may be because the mechanisms for driving the processes involved in nucleating new grains are not well understood. Classical nucleation theory has been applied and found wanting and in real materials segregation and precipitation are often dominant in controlling the microstructural evolution.

5.2 THE DRIVING FORCE FOR PRIMARY RECRYSTALLISATION

It is usually stated that plastic strain energy is the driving force for recrystallisation, but it is not as simple as that. Incubation times are reduced for higher levels of cold work, but recovery processes remove most of the strain energy prior to any recrystallisation. In fact recovery is probably a necessary prelude to the nucleation of the recrystallising grains.

Classical nucleation theory, as already described for precipitate nucleation, requires an embryo created by some thermal fluctuation to exceed some critical size and start to grow ie the free energy change is

$$\Delta G_T = 4\pi r\, \gamma_{gb} - 4\pi r^3 \Delta G_v/3,$$

with a critical radius for growth is:

$$r_c = -2\gamma_{gb}/G_v,$$

and the free energy barrier that must be overcome is:

$$\Delta G_T^* = 16\pi\, \gamma_{gb}/3G_v^2.$$

In this case ΔG_v is the stored plastic energy from the cold work.

An alternative approach is to look at nucleation of new grains by the coalescence of sub–grains. In some cases sub–grain coalescence will result in the formation of a high angle boundary. Such a high angle boundary is likely to have a higher interfacial energy but also a higher mobility. In a few cases when such grains are formed they are large enough to grow, rather than shrink and their driving force for growth will be the absorption of sub–grains, see Fig 5.1. It should be noted that the growth of sub–grains is probably limited by dislocation climb and cross–slip processes, in which intrinsic grain growth is only limited by diffusion across the thickness of the boundary. An estimate of the sub–grain interfacial energy is:

$$\gamma_{sb} = \mu b^2 \rho_b d/6.$$

After deformation $\rho_b \sim (\tau/\mu b)^2$ and $d \sim (10/\rho_b^{\frac{1}{2}})$. This gives an estimate of the sub–grain energy as a function of stress or strain through the work hardening relation:

$$\gamma_{sb} \cong 10b\tau/6.$$

The grain boundary interfacial energy is typically 0.5 J/m^2, compared with the sub–grain boundary energy which is expected to lie in the range 0.03 to 0.2 J/m^2, depending on the degree of cold work. This corresponds to an energy density of $\sim 6\tau^2/\mu$ ie 10^6 to 3.6×10^7 J/m^3, which is comparable to stored energy measurements in deformed metals. A grain nucleus would in general terms only have to be a factor of 2 to 10 larger than the local sub–grain boundary size in order to grow. The incubation time for primary recrystallisation nucleation will be determined by the timescales of sub–grain evolution:

$$\frac{d}{dt} d = 8\mu b^2 \rho_b M_{sb}/3$$

if no precipitates are present and M_{sb} is controlled by either dislocation pipe diffusion or by lattice diffusion. Nucleation should occur when d has increased in size by a factor of 2 to 10.

5.3 PRIMARY RECRYSTALLISATION AND PRECIPITATION

Precipitation can affect primary recrystallisation in many ways. If the precipitate distribution is fine enough it can anchor the sub–grains and prevent sub–grain growth. Some slow evolution of the sub–grain structure may occur or more likely recrystallisation has to wait until the precipitate density ahs coarsened sufficiently to release the sub–grains. Irradiation can play a role in this as precipitate coarsening rates can be considerably enhanced by radiation resolution of precipitates and enhanced diffusion rates.

Large precipitates or inclusions can also provided sites for primary recrystallisation nucleation, see Fig 5.2. Large hard precipitates act as barriers to dislocations and also provide sites for local stress concentrations. The larger the particle the more likely that recrystallisation will be nucleated in the vicinity of the particle. It is generally observed that the recrystallisation nucleate at sub–grains close to but not at the particle surface. Often recrystallisation nucleated in this way will continue unti l it covers the deformed zone around the particle and then stops, see Fig 5.3.

The subsequent growth of grains once they have been nucleated will be determined by the grain boundary mobility and the driving force provided by the sub–grain structure. The pressure driving the grain growth is:

$$p_{gb} = \frac{\gamma_{sb}}{d} - \frac{\gamma_{gb}}{D} \simeq \mu\, b^2 \rho_b/6,$$

which is essentially constant during the growth. hence the kinetics are predicted to be that which is observed where

$$G = v_{gb} = M_{gb}\, \mu\, b^2\, \rho_b/6.$$

M_{gb} will be determined by the intrinsic mobility, solute drag values or particle mobility as appropriate.

The experimental observation of grain size after primary recrystallisation is that the grain diameter is smaller for larger amounts of cold work strain. This corresponds well with the

model of nucleation from sub–grain coalescence, where we would expect the number of grain nuclei to be directly related to the original sub–grain density, ie inversely related to the sub–grain diameter. Where primary recrystallisation is nucleated at large particles, the recrystallised grain size will be proportional to particle spacing.

For small particles, if the particle spacing is small compared to the sub–grain size and particles are dragged as the grain grows, the task gets harder as time increases. The area occupied by particles decreases and the grain boundary mobility will markedly diminish. Where the particle spacing is wide, the grains may be undented between particles. The grains will grow until they touch the particles. At this grain growth may cease if the driving force for growth is insufficient, ie if:

$$p < 12\, f\, \gamma_{gb}/r_p.$$

Further grain nucleation may occur before particle mobility or ripening will permit further grain growth. This will put an upper limit to the grain size to approximately the particle spacing.

5.4 GRAIN GROWTH AND SECONDARY RECRYSTALLISATION

In the previous lecture we have described in some detail the factors influencing grain boundary mobility. In this lecture we will look at the grain growth subsequent to primary recrystallisation and compare the driving forcs with those for normal grain growth.

Normal grain growth is a more or less uniform increase in grain size that arises from the smallest grains in the size distribution shrinking at the expense of their neighbours. The driving force is the resulting decrease in grain boundary energy. Usually a spherical grain boundary model is used to derive the driving, but there are geometric considerations to be taken into account. In fact for a two–dimensional array of grains a stable polygonal grain

structure can be established. For three–dimensional grains this is not possible, although the grains are polyhedral in geometry. This is because no boundary can have the ideal tetrahedral set of angles at all its nodes. Such geometrical effects can influence grain stability and it is not always the smallest grain that shrinks.

The simplest treatment of normal grain growth just models pressure driving growth as a function of the mean grain size, ie:

$$p = C\,\gamma_{gb}/D$$

where C is a constant greater than 1 reflecting that the grains shrinking will be smaller than the average. The grain growth rate is then proportional to the velocity of the boundary:

$$\frac{dD}{dt} = C'\,M_{gb}\,\frac{\gamma_{gb}}{D}$$

or

$$D^2 - D_0^2 = Kt,$$

which is known as the parabolic grain growth law. The parabolic growth law can be derived from more complicated analyses that take into account a realistic distribution of grain sizes. In particular a Fokker–Plank equation can be written to represent the redistribution of grain size. Feltham and Hillert use just the drift term

$$\frac{\partial f}{\partial t} + \frac{\partial}{\partial D}(f\,v_{gb}) = 0,$$

where f(D,t) is the grain size distribution function. The problem is essentially the same as that for ripening of precipitates. Computer simulation techniques are currently being developed that permit a more realistic simulation of a limited population of grains. Monte–Carlo models are commonly used. The results of three–dimensional models, made possible for usefully sized lattices by super–computer, indicate kinetic with higher power laws than the parabolic law:

$$D^n - D_0^n = kt$$

where n lies between 3 and 4. This is close to observation values.

Higher values of m can be derived when the mobility of the boundaries is dependent on drag of precipitates or pores. The mobility of a boundary sweeping up precipitates will diminish rapidly. The value of m will depend on whether there is coalescence of particles. If there is no coalescence and the precipitates are uniformly distributed we might expect n to lie between 4 and 6, which is the observed range.

This type of normal grain growth is usually only seen at the end of what is known as secondary recrystallisation. In secondary recrystallisation, the relatively fine distribution of grains grows by a few grains absorbing the rest. In a similar manner to growth during primary recrystallisation the growth rate is constant after an incubation period. This is because the driving force for growth remains constant once the cannibal grains start to eat the others:

$$p = \gamma_{gb}/D_{pc}$$

where D_{pc} is the mean grain size at the end of primary recrystallisation. The anticipated grain growth rate is simply:

$$\frac{dD}{dt} = M_{gb}\gamma_{gb}/D_{pc}.$$

Secondary recrystallisation may in fact start with normal grain growth but the very large driving forces involved may lead to an instability. It is also possible that some grain boundary relationships have a particularly favourable orientation for growth which causes a few grains to grow rapidly initially and nuclear the abnormal growth. If such relationships are rare the possibility of a few occurring in a sample is more likely when the grain size is small.

The presence of a solute segregated to boundaries may also destabilise the grain growth. A grain that can break away from its solute could grow rapidly and again nucleate abnormal growth. However, there are special features of the grain distribution after

primary recrystallisation that may predispose the grains to abnormal growth. Firstly, the random nature of the primary recrystallisation nucleation process will lead to a distorted grain size distribution which will have a few grains much larger than expected from a normal distribution. Secondly, the grains after primary recrystallisation will tend locally to have a pronolunced texture arising partly from the deformation process and partly from the original unrecrystallised grain structure. This texture also appears to destabilise growth.

The relationships for pinning of grain boundaries during abnormal grain growth are different from those in normal growth. The critical size for a grain to grow by abnormal growth derived by Rios is:

$$D_{AC} > D_{pc}/[3(1-D_{pc}f/rp)].$$

Rios has derived a map relating the probability of normal growth, abnormal growth and pinning to the size distribution of the grains, see Fig 5.4. Precipitate pinning can destabilise grain growth in a similar way to solute segregation.

5.5 DYNAMIC RECRYSTALLISATION

In Lecture 1 we have outlined the main observations in dynamic recrystallisation. We note here that at high strain rate and large initial grain size continuous dynamic recrystallisation is observed and with grain refinement. For low strainrate and small initial grain size cyclic softening behaviour and grain coarsening are observed. See the map from Sakai and Jones given in Fig 5.5.

Theory to describe these processes is not very well developed. Nucleation of new grains at the grain boundaries is probably related to a smaller sub–grain size adjacent to the boundary, caused by local stress concentrations produced by grain boundary sliding.

Subsequent nucleation of rings of grains propagating inwards from boundary is probably a direct consequence of softening associated with the recrystallised grains. The softened grains deform more and mismatch stresses trigger the next stage of the recrystallisation.

The difference in behaviour between high strain rate and low strain rate hot working is simply related to the timescales for nucleation and growth of the recrystallising grains. At high strain rate a new set of recrystallising grains is nucleated before the first set is fully grown. The grain size is refined until the driving forces for grain growth match the strain rate. At slower strain rates there is time for full secondary recrystallisation before the next round of nuclei are formed. There is a tendency for the whole of the material to be brought into step to produce the strong softening cycles, as any region out of step will harden or soften more rapidly than adjacent regions. Solute effects may enhance the cyclicsoftening by lengthening the incubation period for grain nucleation.

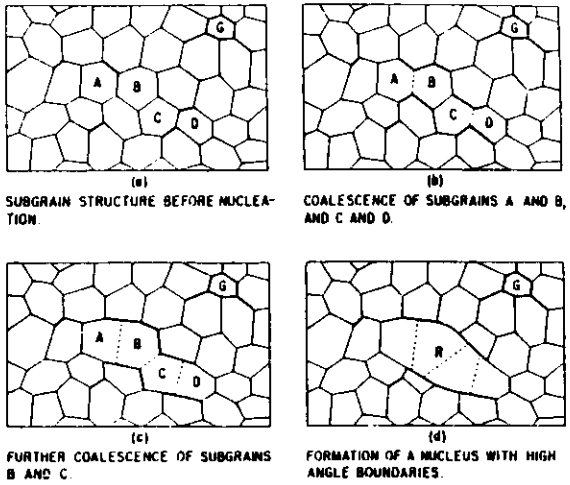

FIGURE 5.1 Schematic representation of the formation of a primary recrystallization nucleus by subgrain coalescence. (After Hu, ref. 244.)

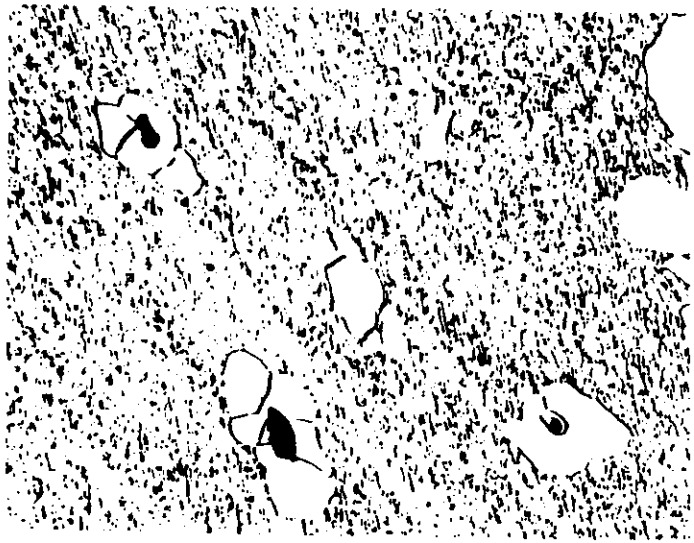

FIGURE 5.2. Recrystallized grains formed at oxide inclusions in iron. (After Leslie *et al.* ref. 196.)
Magnification x 120.

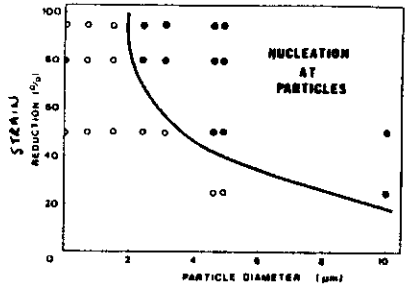

The conditions of strain and particle size under which particle stimulated nucleation occurs in Al-Si. (Humphreys 1977).

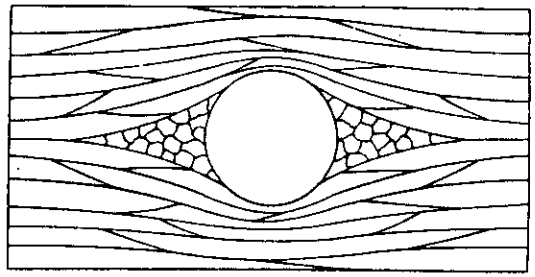

Fig. 5.3 Schematic diagram of subgrain structure around SiO_2 particles in cold rolled copper (Porter and Humphreys 1979).

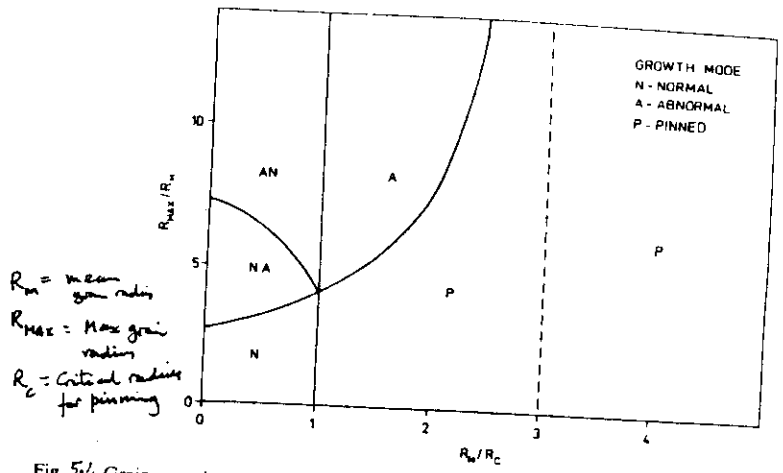

Fig. 5.4 Grain growth mechanism map. R_{max}/R_M is the heterogeneity present in the system. R_M/R_c is the matrix grain radius divided by the critical grain radius. For detailed explanation see text.

(Ross)

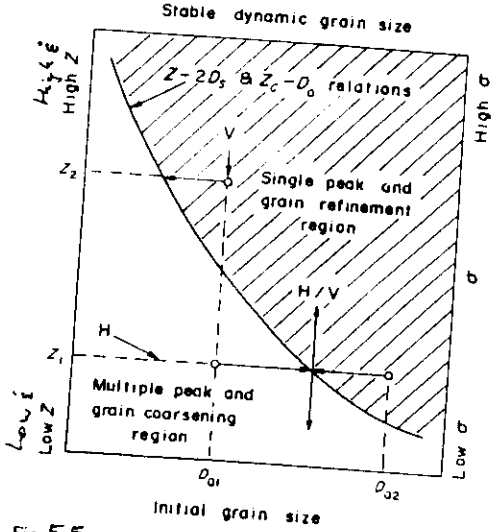

Fig. 5.5 A microstructural mechanism map for distinguishing between the occurrence of two types of dynamic recrystallization. The curve describing the $Z=2D_s$ and $Z_c=D_0$ relations separates the single (grain refinement) from the multiple peak (grain coarsening) region. Three distinct types of experiment are represented: "vertical" tests (V) carried out over a range of strain rates and temperatures on material with a *fixed* initial grain size D_{01}; "horizontal" tests (H) carried out at a fixed temperature-compensated strain rate Z_1 with a series of initial grain sizes in the range D_{01} to D_{02}, combined "horizontal/vertical" (H V) tests involving changes in strain rate or temperature after a period of steady state deformation [34, 36].